Modeling ^{230}Th (and ^{231}Pa):

As an approach to study the intermediate and deep water circulation in the Arctic Ocean

by

Xiaoxin Yu

B.Sc., Sun Yat-Sen University, 2014

A THESIS SUBMITTED IN PARTIAL FULFILLMENT OF
THE REQUIREMENTS FOR THE DEGREE OF

MASTER OF SCIENCE

in

The Faculty of Graduate and Postdoctoral Studies

(Oceanography)

THE UNIVERSITY OF BRITISH COLUMBIA

(Vancouver)

April 2017

Abstract

Recently observed ^{230}Th concentrations in 2007 and 2009 documented very high ^{230}Th values within the Atlantic layer in the Canada Basin of the Arctic Ocean. Similar levels of high ^{230}Th had only been previously observed in the Alpha Ridge region, implying that the Alpha Ridge is the potential source of the high ^{230}Th waters. As the Alpha Ridge is downstream in the classic cyclonic circulation, that circulation is believed to have changed. Motivated by this, a three-dimensional Arctic ^{230}Th model is configured for the first time to study such change.

To simulate the tracer, I coupled a scavenging model, which describes the exchange of ^{230}Th (and ^{231}Pa) between the dissolved and particulate phases, to an offline NEMO model (the Nucleus for European Modelling of the Ocean) that provides the advection and mixing processes that redistribute the tracers within the ocean. As the scavenging rates of such tracer elements are strongly affected by oceanic particle concentrations, the scavenging rates are parameterized as a function of ice concentration, which, to a great extent, influences the biological processes in the water.

Model output produced an increase of ^{230}Th concentration in the south Canada Basin. Sensitivity experiments confirm such change is not caused by a change in the particle field but a change in the intermediate circulation from cyclonic to anticyclonic throughout the Amerasian Basin. This shift in circulation is the reason for a subsequent transport of high ^{230}Th concentration from the Alpha Ridge to the south Canada Basin.

The model circulation and density fields suggest that the change in the flow is caused by increased dense water flux into the Arctic Ocean, primarily through the Barents Sea route. This increase of dense water inflow alters the density distribution in the Arctic and results in a quick adjustment in the Atlantic layer ($\sim$ 1 year) through propagation of boundary trapped internal Kelvin waves.

Preface

This project was initiated by my supervisor Dr. Susan Allen. This thesis is an original work of the author, X. Yu. The observations reported in this thesis have two sources: the previously published data and unpublished data from Dr. Roger Francois, Dr. Michiel van der Loeff, Dr. Melanie Grenier and Ole Valk (Grenier et al., in prep.; Valk et al., in prep.). The physical model outputs from the ANHA4 (Arctic and Northern Hemisphere Atlantic) configurations, which were applied to force the tracer model and to investigate the physics behind the change in the Arctic intermediate circulation pattern, are provided by Dr. Paul Myers and Xianmin Hu from University of Alberta.

Table of Contents

List of Tables

List of Figures

Acknowledgments

First and most importantly, I would like to thank my advisor Dr. Susan Allen, for all the support throughout this work. Thanks for your guidance, encouragement and invaluable suggestions along the way. It has truly been a pleasure to be one of your students.

I would also like to thank my committee members, Dr. Roger Francois and Melanie Grenier, for all insightful discussions and helpful feedback.

Special thanks to everyone in the Waterhole with whom I have shared endless discussions and to Doug Latornell for all technical help on Jasper, Python and Mercurial.

Last but not least, I would also like to acknowledge my family, especially my parents, and Ryan. I couldn't possibly express all the thanks I have for you. Because the list is endless.

Chapter 1

Introduction

1.1 Recent changes in the Arctic Ocean

The Arctic Ocean is recognized as an important component of the global circulation. It takes an Atlantic input, densifies it and returns it back to the Atlantic. The modified water mass is an important component of meridional overturning circulation (Rudels and Friedrich, 2000). As the overturning circulation plays a crucial role in the global varying climate through transporting heat around the world (Delworth et al., 2008), the Arctic ocean is not only crucial to local people there, but to all of us.

The Arctic Ocean is traditionally studied as a three-layer system: the surface layer, the intermediate layer (also known as Atlantic layer) and the deep layer, which are separated by isopycnal $\sigma_\theta = 27.8$ at around 400 m and ispycnal $\sigma_\theta = 28.0$ at around 1500 m, respectively (Lique et al., 2010). The warm, saline Atlantic layer serves as an important source of heat and salt transport to the Arctic Ocean. Any change in this layer significantly impacts the Arctic surface layer, as well as the return flow back to the Atlantic Ocean.

Important as the Atlantic layer is, efforts have been made in understanding its circulation in the Arctic. The classic intermediate circulation pattern includes three cyclonic gyres inferred from the analysis of hydrographic observations (Rudels et al., 1994) . The first cyclonic gyre is in the Eurasian Basin: it receives inflows from Fram Strait and the Barents Sea, transports this water along the Lomonosov Ridge and returns it to Fram Strait. A fraction of the inflows (mainly from the Barents Sea branch), however, crosses the Lomonosov Ridge (Rudels et al., 1994) and develops into two cyclonic gyres in the Canada Basin and the Makarov Basin. These flows eventually exit the Arctic Ocean through Fram Strait (Fig 1.1).

However, this classic intermediate circulation is not stable. A recent study on geo-tracer ^{129}I revealed the circulation pattern in the Canada Basin changed from cyclonic to anticyclonic, as implied by the arrival in 2007 of a large ^{129}I spike (Karcher et al., 2012). Similarly, another geo-tracer study, ^{230}Th, also reported that, in contrast to the previous ^{230}Th profile measured in the Canada Basin that displayed a linear increase in concentration with depth (Edmonds et al., 1998), an observed ^{230}Th profile in 2007 surprisingly documented very large deviations from linearity within the Atlantic Water. These deviations imply that recent changes occurred in the Atlantic layer of the Canada Basin (Francois and Soon, 2010).

However, while the observations point to pronounce changes, the forcing mechanism in the Atlantic layer remains unclear. Originally, it was suggested, by an idealized barotropic model, that the Atlantic flow pattern was mainly driven by the lateral transport of positive potential vorticity (PV) (Yang, 2005). Later, a study proposed that vertical PV flux, closely related to wind field changes, was a more important factor (Karcher et al., 2007). They found that half the variance of Atlantic Water (AW) layer of the Amerasian Basin could be explained by the wind forcing. Zhang and Steele (2007) also emphasized the importance of the vertical mixing process in simulating the direction and intensity of the AW circulation. However, recent studies suggested that changes in the vertical mixing only significantly altered the depth of the halocline but not the AW circulation (Lique et al., 2015; Spall, 2013). Spall (2013) further showed that the ultimate driving force for the Atlantic Water in the model was the salinity contrast between the Atlantic water and the Arctic shelves.

Motivated by the observed changes in the tracer profiles and the unsolved puzzle in the forcing mechanism, this thesis aims at exploring the ongoing changes in the intermediate layer of the Arctic Ocean from a geo-tracer perspective.

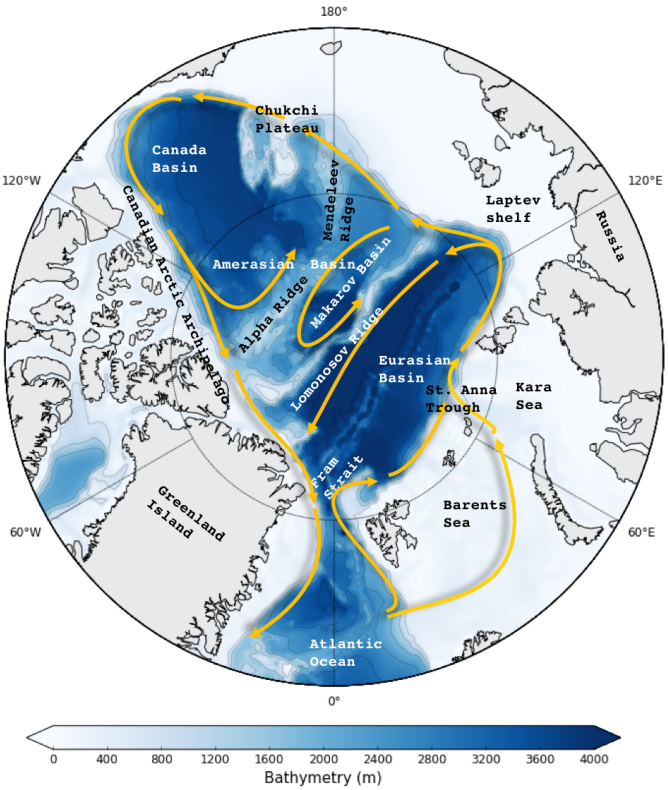

Figure 1.1: Bottom topography and schematic of the Atlantic Water circulation in the Arctic Basin (modified from Spall (2013)).

1.2 ^{230}Th and ^{231}Pa as tracers

Recent warming of the climate opens up the possibility of taking measurements in the Arctic. However, as the existing velocity data in the Arctic does not have good spatial and temporal coverage, this study does not directly apply velocity measurements to study the recent change in the Atlantic layer, but uses a tracer method.

Traditional tracers for ocean circulation are temperature and salinity. However, in the intermediate Arctic, variations in temperature and salinity are generally small. As such, a long-lived, highly particle-reactive isotope, ^{230}Th, is better suited for Arctic circulation studies because of its large spatial variations caused by the large contrast in productivity between the seasonally ice-free shelves and the perennial ice-covered deep basins. This isotope is commonly studied with ^{231}Pa and their ratio is a promising proxy of oceanic processes in both the present and past marine environment (Marchal et al., 2000; Yu et al., 2001).

Geochemical cycles for ^{231}Pa and ^{230}Th are very similar, however, their usefulness as tracers of ocean circulation is mainly a result of the difference in particle reactivity between ^{231}Pa and ^{230}Th in the water column - ^{231}Pa has a higher affinity for biogenic opal and authigenic manganese oxides compared with the other major sedimentary components, such as calcium carbonate and clay/lithogenic material (smaller in size), while ^{230}Th is scavenged more equally among different particle types (Bacon and Anderson, 1982). This difference in particle affinities results in a significant difference in their oceanic residence time (20-40 years for ^{230}Th, 100-200 for ^{231}Pa (Yu et al., 2001)).

The ^{231}Pa/^{230}Th ratio is most extensively applied in understanding the Atlantic Meridional overturning circulation because ^{231}Pa can be advected further south than ^{230}Th, which leads to variations in the ^{231}Pa/^{230}Th ratio. Consequently, the ratio recorded in sediments preserves information on ventilation rate and geometry of the overturning circulation in the past, while that in the water column helps to constrain the long term mean, present circulation.

The second most popular ^{231}Pa and ^{230}Th application is in the Arctic. In the 1990s, chemical oceanographers used observed distributions of ^{230}Th and ^{231}Pa in the Arctic to explain the basin-scale ventilation rates (as well as the pronounced differential scavenging) (Scholten et al., 1995). However, studies of ^{231}Pa and ^{230}Th discontinued in late 1990s. It was not until the 2007 Arctic explorations of the Wilfried Laurier and the Polarstern that the observations of these isotopes restarted.

While ^{231}Pa/^{230}Th has been widely used in the ocean, an interesting question to ask is if the information provided by ^{231}Pa/^{230}Th can be acquired from only one of these elements. If we take a step back and reconsider why ^{231}Pa/^{230}Th can be used as a circulation proxy, we can find the long travel distance of ^{231}Pa is the main reason. Compared to the large scale overturning circulation, the spatial scale of the Arctic circulation is much smaller, to such a degree that the travel distance for

^{230}Th is sufficient to indicate the Arctic water pathways. An argument to support this is that the residence time of ^{230}Th in the water column, approximately 22 years in both the Canada and Eurasian basins and 39-45 years over the Alpha Ridge and in the Makarov Basin (Scholten et al., 1995; Trimble et al., 2004), is of similar magnitude to the travel time (∼30 years) of the intermediate water in the Arctic (Lique et al., 2010).

Consequently, ^{230}Th alone is sufficient to act as a circulation proxy in the Arctic Ocean. In my master's research, the distribution of ^{231}Pa and ^{230}Th are both simulated. However, for the reason mentioned above, this thesis presents only simulated ^{230}Th results. The results for ^{231}Pa are shown in Appendix D.

1.2.1 Geochemical behavior of ^{230}Th (and ^{231}Pa)

^{230}Th (and ^{231}Pa) is added to seawater by the decay of Uranium isotopes with a constant production rate (Fig. 1.2). The dissolved phases are removed from the water column by attaching to marine particles, through a process known as scavenging, and sink with marine particles in the particulate form. Since the exchange between the dissolved and particulate phase is reversible, the particulate phase will also desorb from particles and return to water column as they sink. Such exchange occurs continuously until the marine particles eventually reach the seafloor. Meanwhile, currents play an important role in redistributing the tracers over the ocean.

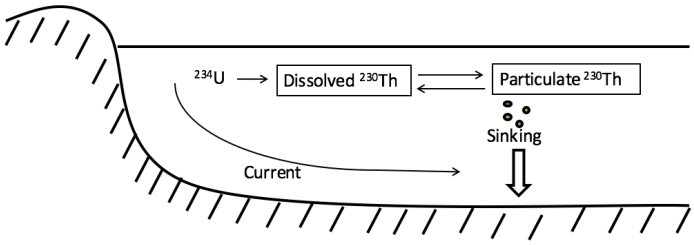

Figure 1.2: Conceptual map: ^{230}Th cycle in the ocean.

1.2.2 Modeling study of ^{230}Th (and ^{231}Pa)

With more ^{230}Th observations available, many recent efforts have been made to model the ^{230}Th (and ^{231}Pa) distribution in the ocean. The typical way to simulate the tracer is to couple a chemical scavenging model to a physical flow field, with scavenging coefficients estimated from observations (Dutay et al., 2009; Lerner et al., 2016; Luo and Lippold, 2015; Marchal et al., 2007, 2000; Roy-Barman, 2009).

However, most of the models tend to underestimate the potential complexity of the system by using a vertically uniform particle sinking velocity and constant scavenging coefficients. The former simplification implicitly assumes no variation

in the particulate tracer field which is not supported by observations. The latter is also not appropriate given rapidly changing biology fields.

Lately, improvements were made (Dutay et al., 2009; Lerner et al., 2016) to simulate ^{231}Pa and ^{230}Th distribution by generating the scavenging coefficients based on simulated particle fields. Although some large deviations between the observations and their simulations remain, the allowance of vertical and spatial variations in the scavenging coefficients lead to a significantly better fit to the data. This method was used as inspiration for the modeling of tracers in this study.

1.3 Thesis objectives

In this study, a three-dimensional, Arctic ^{230}Th (and ^{231}Pa) model is configured for the first time.

I couple a scavenging model, which describes the exchange of ^{230}Th (and ^{231}Pa) between the dissolved and particulate phases, to an offline ocean dynamics model (the Nucleus for European Modelling of the Ocean - NEMO) that provides the advection and mixing processes that redistribute the tracers within the ocean to simulate the tracer distributions in the Arctic ocean. In this attempt, the scavenging coefficients are not treated as constants but vary spatially and vertically based on particle concentrations.

This study addresses the following research questions:

1. Can the model produce the observed change of ^{230}Th? What does the observed change imply about the Arctic circulation?

2. What is the reason for the circulation changes in the Atlantic water layer in the Arctic?

This thesis is organized as follows. Chapter 2 gives a detailed description of the model construction. Chapter 3 presents the tracer model results and analyzes the physical flow fields. Further implications of the results will be discussed in Chapter 4. A summary section is provided in Chapter 5.

Chapter 2

Methods

2.1 Model structure and regional Arctic configuration

To model the tracer distribution, the Nucleus for European Modelling of the Ocean (NEMO v3.4) is used with two sub-models nested inside: first, a scavenging model which simulates the exchange process between the dissolved and particulate form; second, an ocean dynamics model which transports and mixes tracers within the ocean. More detailed descriptions can be found in Section 2.1.1 and 2.1.2.

The regional Arctic configuration used in this study is the Arctic Northern Hemisphere Atlantic configuration (ANHA4) and was initially configured by University of Alberta for the VITALS (Ventilation, Interactions and Transports Across the Labrador Sea) project based on the NEMO framework. It includes a three-dimensional, free surface, hydrostatic, primitive-equation ocean general circulation model and a dynamic-thermodynamic sea-ice model (Louvain-la-Neuve: LIM2). Note that there is no tidal forcing implementation in current configuration.

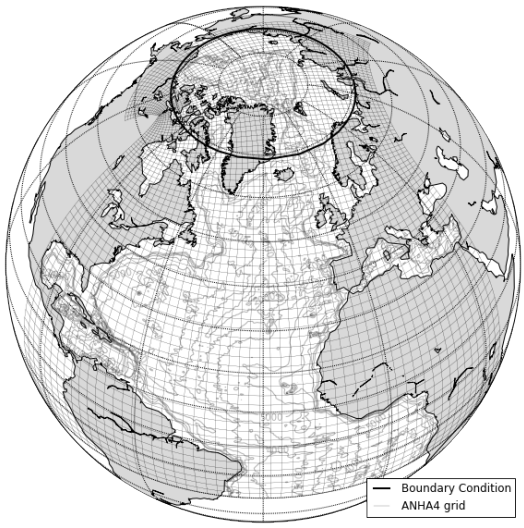

Figure 2.1: Model grids for the ANHA4 configuration. The grid is plotted every 10 grid points. The contours are the bathymetry. The black circle at latitude 70° delimits the tracer boundary.

The ANHA4 configuration is contained within open boundaries at 20°S latitude

in the Atlantic and across the Bering Strait. It has a quarter-degree horizontal resolution (Fig. 2.1), with the highest horizontal resolution located in Dease Strait (near the artificial pole over northern Canada), and the lowest resolution at the equator. In the vertical, it uses 50 levels with layer thickness smoothly increasing from 1.05 m at the surface to 453 m at the deepest level. To ensure model stability, the time step is set to be 1080 s; NEMO uses a Leapfrog algorithm for time-stepping.

Tracer transportation is simulated by the total variation diminishing scheme (TVD). For tracer lateral diffusion, an isopycnal Laplacian operator with a horizontal eddy diffusivity of 300 m^2s^{-1} is applied. Vertical mixing uses a turbulent kinetic energy dependent vertical diffusion (TKE) scheme that was parameterized using a second-order turbulent closure scheme. The model bathymetry is derived from 1-minute gridded elevations/bathymetry for the world (ETOPO1) data. Partial z-steps are utilized to better resolve the sea floor.

The ANHA4 configuration has been successfully applied to study several freshwater processes in the Arctic regions, as well as circulation and deep convection of the Labrador sea (Holdsworth and Myers, 2015). In this study, it is applied to both the physical fields and the scavenging model.

2.1.1 Physical model

Five-day model outputs from University of Alberta are used as our ocean dynamic inputs. Among available ANHA4 runs, I chose two velocity fields, EXH001 and EXH005, to conduct this study (Table 2.1). These two simulations were initialized with Global Ocean Reanalyses and Simulations (GLORYS) data, ran with river runoff taken from the 12-month climatological data of Dai and Trenberth (2002) and forced by interannual atmospheric data from CMC GDPS reforecasts (CGRF) (Smith et al., 2014).

It is particularly interesting to conduct studies on these two runs because they are forced by the same input files, except for the precipitation field, but the modeled velocity fields turn out to be surprisingly different. To be specific, the EXH001 boundary currents in the Arctic intermediate layer shifted from cyclonic to anticyclonic during the run, while those in EXH005 remained cyclonic over the entire model period.

Simulation	Integration	Initial condition	Climatology forcing
EXH001	2002-2014	GLORYS2v3	CGRF(less precipitation)
EXH005	2002-2014	GLORYS2v3	CGRF(more precipitation)

Table 2.1: Summary of ANHA4 runs used in this thesis. More details can be found at (http://knossos.eas.ualberta.ca/xianmin/anha/anhatable.html).

The contrast between these two runs in terms of circulation pattern will be used to understand how the tracers respond to currents. Meanwhile, the temperature,

salinity and velocity fields from these runs will be applied to investigate what contributes to the change in circulation pattern.

2.1.2 Scavenging model

The second component needed in this study is a reversible scavenging model (Bacon and Anderson, 1982). The tracer scavenging processes are controlled by absorption, desorption and sinking. Provided tracer concentrations are in dissolved form x_d and particulate form x_p, they are described by the following equations:

$$\frac{\partial x_d}{\partial t} = q - k_a x_d + k_d x_p + advection + mixing \tag{2.1}$$

$$\frac{\partial x_p}{\partial t} = k_a x_d - k_d x_p - s\frac{\partial x_p}{\partial z} + advection + mixing \tag{2.2}$$

where q (dpm $m^{-3}y^{-1}$) is the production rate of ^{230}Th, k_a (y^{-1}) and k_d (y^{-1}) are the exchange rate constants of ^{230}Th by adsorption and desorption respectively, s (m y^{-1}) is the sinking rate of particles and z (m) is vertical depth, positive upward. These equations neglect the radioactive decay of ^{230}Th itself (^{230}Th half-life: 75000 years).

Production rate, q, sinking rate, s, scavenging coefficients k_a and k_d together control the tracer vertical distributions. Among all these parameters, the production rate is the best known (0.0267 dpm $m^{-3}y^{-1}$ for ^{230}Th), while the rest are left to be determined. (Same situation for ^{231}Pa. Details and results can be found in Appendix D.)

2.2 Tracer parameterization

The main challenge of this work is constructing a spatial distribution of scavenging intensity within the model domain based on existing ^{230}Th data. The following section first introduces data used in the parameterization, then describes methods to determine scavenging intensity at each sample location and finally presents an approximation method to interpolate the scavenging coefficients from isolated sample locations to the entire Arctic domain.

Observations

I use water column particulate and dissolved data obtained from a dataset compiled by Henderson and Wilkinson (2012) to constrain the unknown scavenging rates in this thesis. The data mainly come from cruises in 1983 and 1991 (Fig. 2.2).

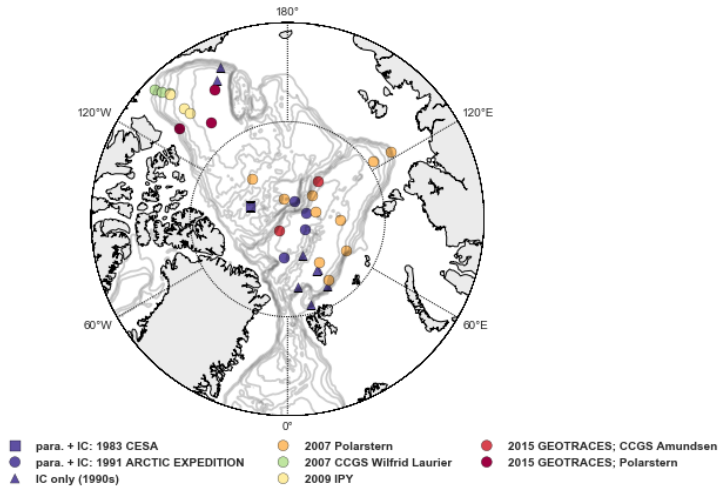

Figure 2.2: ^{230}Th measurements over the Arctic regions. Data are available for the Canada Basin, Alpha Ridge, Makarov Basin and Eurasian Basin. Data from cruises 1983 and 1991 are used in the parameterzation (para.) and initial conditions (IC), while those measured in 2000s are used in model evaluation (section 3.2).

Determination of scavenging rates at sample locations

Assuming that the tracer profile is at steady state and that advection and mixing processes are negligible, the solutions of (2.1) and (2.2) are:

$$x_p = \frac{q}{s} z + c \tag{2.3}$$

$$x_d = \frac{q}{k_a} + \frac{k_d}{k_a} \left(\frac{q}{s} z + c \right) \tag{2.4}$$

where c is an intercept from integrating (2.1). If the effect of the mixed layer is neglected, particulate ^{230}Th produced at $z = 0$ tends towards 0, which gives the surface boundary condition, $c = 0$.

The linearity of the tracer analytic solutions (2.3) and (2.4) enables us to estimate the scavenging coefficients through a least square regression. To ensure that high-quality data influences the regression more than low-quality data, a weighted least square regression technique is applied; data is weighted by measurement errors reported in the original publications.

Equation (2.3) suggests that steady state particulate element concentrations are proportional to the inverse of its sinking rate. Given that the slope of particulate phase determined by linear regression is $\alpha_p \pm \epsilon_{\alpha_p}$, the sinking rate s can be estimated.

$$s = \frac{q}{\alpha_p} \tag{2.5}$$

The corresponding error is estimated by error propagation rules (Ku, 1966):

$$\epsilon_s = s\sqrt{\left(\frac{\epsilon_{\alpha_p}}{\alpha_p}\right)^2} \tag{2.6}$$

Similarly, (2.4) indicates that the dissolved element has an intercept that is inversely related to the adsorption rate and a slope that is controlled by the sinking velocity and the ratio of desorption rate and adsorption rate. Provided the linear regression slope for dissolved phase is $\alpha_d \pm \epsilon_{\alpha_d}$, the ratio of adsorption rate over desorption rate can be estimated:

$$\frac{k_a}{k_d} = \frac{q}{\alpha_d s} = \frac{\alpha_p}{\alpha_d} \tag{2.7}$$

The corresponding error is:

$$\epsilon_{\frac{k_a}{k_d}} = \frac{k_a}{k_d}\sqrt{\left(\frac{\epsilon_{\alpha_p}}{\alpha_p}\right)^2 + \left(\frac{\epsilon_{\alpha_d}}{\alpha_d}\right)^2} \tag{2.8}$$

However, (2.7) only provides a relationship between absorption and desorption rates. Inspired by an early study (Bacon and Anderson, 1982), which found a strong positive correlation between the adsorption rate coefficient and suspended matter concentration but did not find such dependence in desorption rate, I treated ^{230}Th desorption rates as a constant over the Arctic domain. Therefore, the absorption rate can be calculated:

$$k_a = k_d \frac{\alpha_p}{\alpha_d} \tag{2.9}$$

This simplification on k_d decreases the degrees of freedom such that the analytical solution fits the slope but not the intercept and thus creates a uniform in depth discrepancy between the observation and the analytical solution (Fig. 2.3). This discrepancy can be quantified by the difference in the intercept between the observation and the analytical solution, Δc.

$$\Delta c = \beta_d - \frac{q}{k_a} \tag{2.10}$$

in which β_d is the linear regression intercept from the observed profiles; q/k_a is the intercept from the analytical solution.

As such, with an iteration on (2.7) for all stations (or groups if one groups some stations together), the sum of Δc ($\sum \Delta c$) from all stations (or all groups) can be used to find the best k_a by searching for a k_d that minimizes the total discrepancy between all observations and analytical solutions.

Selecting the data

However, one obvious disadvantage of this method is that it tends to generate high uncertainty in scavenging intensity when the advection effect is strong compared to particle sinking (Venchiarutti et al., 2008). Stations close to Fram Strait receive strong lateral advection from the Atlantic Ocean (profiles are not linear deeper than approximately 1000 m depth). For this reason, I did not apply data from those locations in the paramerization (marked as triangles in Fig. 2.2).

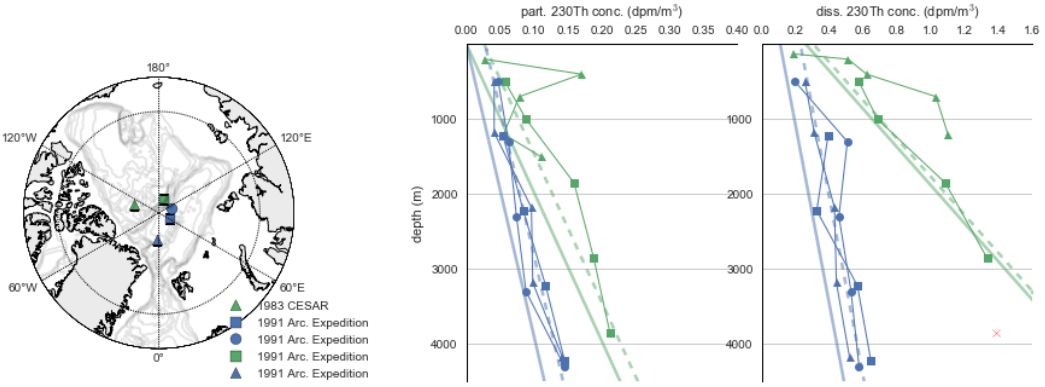

Figure 2.3: Linear regressions of the observed ^{230}Th profiles in the Eurasian Basin and the Alpha Ridge region. The left panel shows a map with observation locations. The middle panel shows linear regressions (dashed lines) on observed particulate ^{230}Th (points). The solid lines are the analytical solutions recalculated from estimated scavenging coefficients; Right panel: same but for the dissolved ^{230}Th profile. Tracer profiles show that ^{230}Th concentrations over the Alpha Ridge and in the Makarov Basin (green) increase with depth faster than those in the Eurasian Basin (blue).

The parameterization method established above was performed based on three Eurasian Basin stations ('EB group') and two central Arctic stations ('AR group'),

one over the Alpha Ridge and one in the Makarov Basin (Fig. 2.3). Since particles in each basin have similar sources, stations that are geographically close are grouped together for a better least squares regression performance.

Fig. 2.4 indicates the intercept discrepancy between observations and analytical solutions is smallest when $k_d = 0.8$ y^{-1}. Therefore, the ^{230}Th desorption rate is set to 0.8 y^{-1} in this study. Estimated magnitudes of k_a are consistent with previous research (Table 2.2). In this study, k_a is 0.24 y^{-1} in the Eurasian Basin, which falls within the range of 0.12 to 0.55 y^{-1}, shown by Trimble et al. (2004). Estimated k_a of the AR group is 0.1 y^{-1}, which is, again, comparable to previously reported values of 0.16 y^{-1} (Bacon et al., 1989).

Although estimated ^{230}Th absorption rates are in good agreement with previous work, the desorption rate, k_d, estimated in this study is much lower than previous estimates which are 1.5 - 4.0 y^{-1} (Bacon et al., 1989). This discrepancy means more particulate phase will stay in the water column as compared to that from Bacon et al. (1989), because less desorption will occur in the current parameterization scheme. However, because adsorption of ^{230}Th onto particles is balanced by losses due to desorption and sinking processes, the lower desorption rate is compensated by a higher particle sinking rate in my parameterization. In other words, even though there is a difference in desorption rate between previous work and this study, the ratio between dissolved and particulate phases is similar due to a more efficient sinking process.

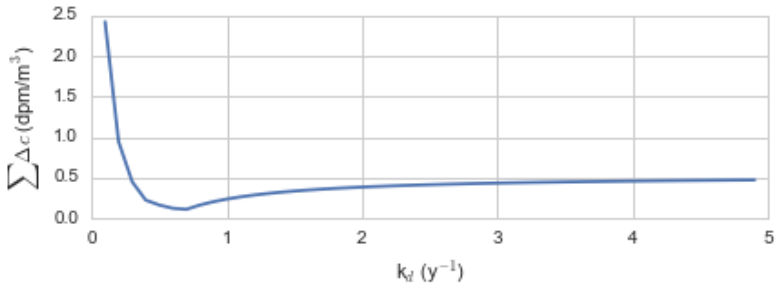

Figure 2.4: Choosing the desorption rate: sum of intercept errors Δc versus k_d. The minimum, k_d= 0.8 y^{-1}, was chosen.

Region	k_a (y^{-1})	s (my^{-1})	k_d
EB group	0.24 ±0.04	1040± 80	0.8
AR group	0.10 ± 0.03	520± 100	0.8

Table 2.2: Scavenging parameters estimated through weighted least squares technique. k_a and k_d are absorption rate and desorption rate, respectively. s is sinking rate. Values are higher for the Eurasian Basin (EB) than for the Alpha Ridge (AR).

Paramerization of scavenging rates over the Arctic

Considering that the distribution of ^{230}Th is closely related to particle concentration distribution (Bacon and Anderson, 1982), and that primary production in the Arctic is strongly affected by sea ice as a result of its control on the light availability (Brown and Arrigo, 2012) (especially by the summer minimum ice, because the major portion of biologic productivity occurs during the summer (Kim et al., 2015)), I conjecture that high biological productivity around the ice free margins of the Arctic Ocean creates a region of enhanced removal of trace elements by scavenging onto particles, while the low biological productivity area that sits under permanent ice produces a region of weak scavenging.

The value of this conjecture lies in the relationship that it implies between the scavenging coefficients and sea ice concentration. The application of this conjecture allows an Arctic-wide scavenging intensity approximation from the horizontal variations of the summer minimum sea ice concentration.

Ice-particle model

However, the influence from the summer minimum sea ice concentration is not immediately reflected in tracer profiles at all depths. Shortly after the time-varying particle fields originate from different sea ice concentrations at the surface, they sink and are advected. As such, to complete the conjecture, it is important to take into consideration this sinking, advection and mixing motion (2.11):

$$\frac{\partial x}{\partial t} = s\frac{\partial x}{\partial z} + \vec{u} \cdot \nabla x + mixing \tag{2.11}$$

where x is the ice fraction that was at the surface when the particle formed. Because particles that scavenge the tracer are assumed to move at same speed as tracer's particulate form, the sinking speed, s, of particles produced at the surface under various sea ice cover is assumed to be identical to the sinking rate of the corresponding particulate tracer. The output from this model is called 'pseudo-particle field' as it tracks the ice fraction that has an implicit relation to the particle concentration. This scheme is expected to capture the variation of scavenging in a changing Arctic.

Scavenging-ice relation

As mentioned above, it takes some time (more precisely, a few years) for the oceanic particles to fall from upper ocean to deeper water, so the surface ice concentration takes years to affect scavenging rates in the deep sea. Therefore, an important step is to determine where particles were initially formed. To investigate this problem, I performed a backward integration of trajectories on NEMO model outputs using Ariane, a particle tracking tool based on an algorithm given by Döös (1995) and Blanke and Raynaud (1997) (http://www.univbrest.fr/lpo/ariane/) (Fig. 2.5).

Initial positions were distributed randomly within the sample locations area. Particles were released at different depths (1000 m, 2000 m and at the seafloor). Because the time coverage of EXH001 and EXH005 is 2002-2014 and the velocity field from the late 1990s to the early 2000s does not have significant change, trajectory calculations are based on the first three years velocity field from EXH001 (2002-2004), with 1.5x velocity speed (the reason for increasing the velocity explained in Section 4.2). Particles are integrated backward in time until they reach the surface. I added an appropriate sinking term of 500 m y^{-1} into Ariane to approximate the sinking process of the marine particles.

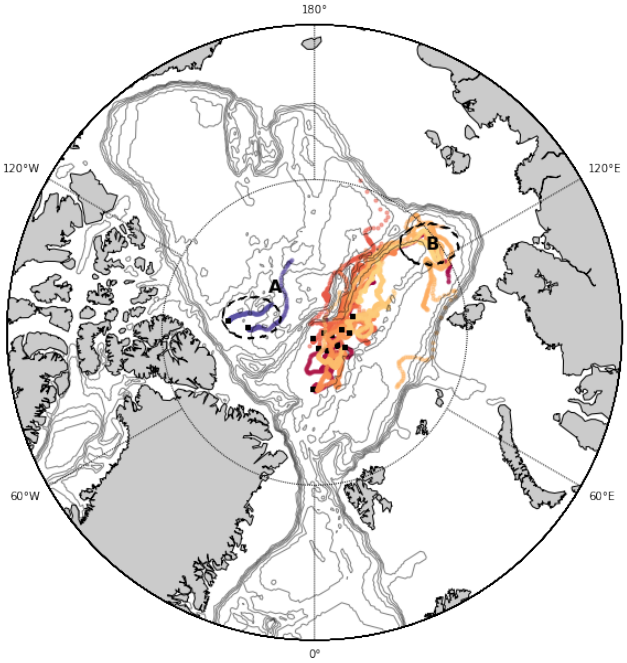

Figure 2.5: Particle trajectories reproduced by Ariane, a computational tool to calculate 3D streamlines from the output velocity field using a Lagrangian analysis. Black points show the initial locations and the lines are the particle trajectories. A and B areas refer to the areas where the particles are initially form in surface (i.e. origin of the seafloor particles of each EB and AR group). Particles in the deep Eurasian Basin are laterally transported from the Laptev side of the Eurasian Basin as they sink, whereas those over the Alpha Ridge move very little laterally.

Judging by the long pathways of particles released in the Eurasian Basin (Fig. 2.5), the sampling locations in the Eurasian Basin are considered to receive strong lateral transportation from the Laptev shelf side of the Eurasian Basin by boundary currents. Since particles released in the central Arctic only moved a few kilometers, the sampling locations from the AR group are treated as places that directly receive

vertical particles from above. This result is consistent with earlier research that shows water masses in the Eurasian Basin interior are carried by slope currents (Pnyushkov et al., 2013), while those over the Alpha Ridge remain in the interior due to weak ventilation (Aagaard, 1989).

Based on this analysis, scavenging coefficients from the Eurasian Basin group (Table 2.2) are related to five-year-averaged sea ice condition from the Laptev shelf side of the Eurasian Basin (location B in Fig. 2.5), while those from the Alpha Ridge group are related to five-year-averaged sea ice condition from the central Arctic (location A in Fig. 2.5).

Information of historical sea ice concentration is taken from NOAA/NSIDC Climate Data Record dataset (Meier et al., 2013; Peng et al., 2013). Satellite-derived sea ice was used instead of the sea ice time series from the model due to bias in the model ice concentration (Appendix A). The averaged sea ice concentration for the Eurasian Basin group and the Alpha Ridge group are 0.62 and 0.97, respectively (Fig. 2.6).

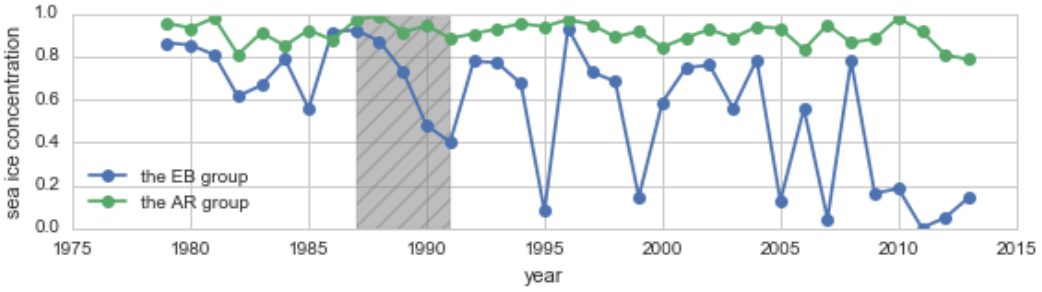

Figure 2.6: Sea ice concentration series over the Alpha Ridge and the Laptev shelf side of the Eurasian Basin from NASA National Snow and Ice Data Center (Meier et al., 2013; Peng et al., 2013). The grey shading shows the potion of the sea ice time series used to estimate the sea ice condition where the particles originally formed.

With these numbers, the linear relation inferred by the conjecture can easily be found. Values for sinking and adsorption coefficients used in this paper are:

$$s = (-1387 \times i + 1874)\ my^{-1} \tag{2.12}$$

$$k_a = (-0.38 \times i + 0.46)\ y^{-1} \tag{2.13}$$

where i is ice fraction from the ice particle model.

2.3 Boundary and initial conditions

2.3.1 Initial conditions

Initializing from zero concentration, the time scale for ^{230}Th to reach equilibrium is on an order of decades. (Take ^{230}Th at 1000 m depth as an example. The average ^{230}Th concentration at this depth is approximately 0.4-0.5 dpm m^{-3} in the Arctic region. With a production rate at 0.0267 dpm m^{-3} y^{-1} and assuming there is no exchange between different phases and no lateral mixing between different water masses, it already takes ^{230}Th at least 15-19 years to accumulate to 0.4-0.5 dpm m^{-3} (Appendix B.1). With the mixing and exchange processes, it takes even longer.) Given the high resolution in ANHA4, obtaining initial conditions by this method is computationally expensive. There are two other options to generate the initial fields: first, initializing the tracer fields from analytical solutions; second, initializing from existing observations.

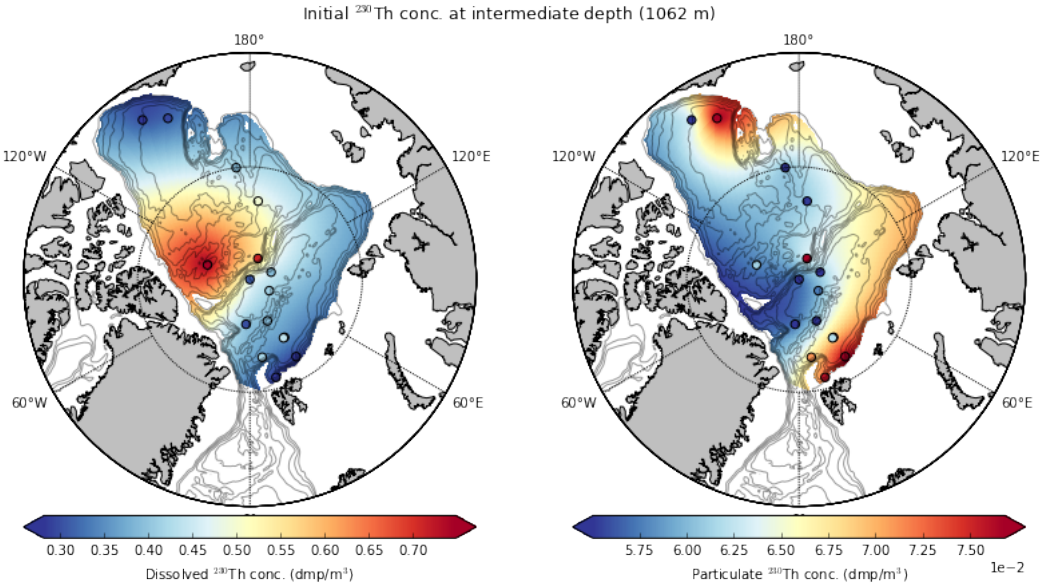

Figure 2.7: Initial conditions for particulate and dissolved ^{230}Th at 1000 m depth. The colored points are observational data. The spatial pattern of dissolved ^{230}Th shows high values in the central Arctic and lower values in the Canada and Eurasian basins.

Generating the initial fields from analytical solutions is quick, however, because the analytical solution assumes the advection is negligible, the corresponding initial field purely reflects scavenging effects. On the contrary, initializing the tracer field with observed data gives an initial ^{230}Th field that will not only reflect particle scavenging, but also the impact of advection.

Given a relatively uniform horizontal distribution of observed ^{230}Th, I generated the initial fields from all available observations measured before 2000 (Fig. 2.7).

Total ^{230}Th data are included in initializing tracer distributions in order to compensate for a lack of spatial coverage of particulate and dissolved data in the Canada and Makarov Basins. To extract dissolved and particulate information from the total ^{230}Th data, I use 90% of the total as the dissolved phase and 10% as the particulate phase since the particulate and dissolved data in the Arctic suggests that the particulate fraction accounts in average for 10-20% of the total ^{230}Th, with the remaining 80-90% in dissolved form.

Vertical linear interpolation was performed to obtain tracer values at the model depths first then a horizontal interpolation on the $\frac{1}{4}\times\frac{1}{4}^{\circ}$ model grid was implemented (Fig. 2.7). The interpolation was performed using PyKrige 0.1.2 Python package (https://pypi.python.org/pypi/PyKrige).

2.3.2 Boundary conditions

The lateral boundaries for the tracer model is 70° N (Fig. 2.1). Tracer values at the boundary are set equal to the initial condition.

Surface boundary condition for the particulate phase is set to 0; for the dissolved phase is set to q/k_a.

The bottom boundary uses the Neumann boundary conditions to constrain the value at the deepest level - the first derivative in the deepest layer concentration is the same as that directly above.

2.3.3 Model Spin-up

The spin-up period is 12 years. There are two reasons for this spin-up length. First, most of the data used in initialization is from 1991. Therefore, spinning up the model for at least a decade enables the tracer to evolve from the 1991 conditions to a 2002 state. Second, there is no significant change in ^{230}Th concentration reported in the Arctic during the late 1990s and the time derivative of the modeled tracer is almost constant after running for this length of time. As such, this spin-up length is considered to be appropriate.

The temporal coverage of EXH001 and EXH005, 2002-2014, does not include 1991-2001. As the circulation pattern does not have significant changes throughout this period, the model is spun up with 2002-2004 circulation repeated four times to give the 12 years.

2.4 Description of numerical experiments

The sensitivity experiments are designed to test contributions from potential affecting factors (Table 2.3). The reference run is forced by flow fields from EXH001; sea ice concentration used for the ice particle model varies based on satellite-derived sea

ice data. The model is run from 2002-2020. Since the physical fields from EXH001 (as well as EXH005) only cover the period of 2002-2014, runs later than 2014 use the 2014 ocean circulation result and sea ice field as dynamic inputs.

The first experiment is designed to investigate tracer sensitivity to ice concentration by holding it constant at 2002 values. It is forced by identical dynamics as that in the reference run. The second experiment is forced by a different flow field (EXH005) to test the tracer sensitivity to circulation. Its sea ice concentration is identical to that in the reference run.

Simulation	Integration	Forcing field	Sea ice
Reference run	2002-2020	EXH001	annual
Exp. 1	2002-2020	EXH001	constant
Exp. 2	2002-2020	EXH005	annual

Table 2.3: Summary of the numerical runs. Runs beyond 2014 repeat the ocean circulation and sea ice field in 2014.

2.5 Methods for analyzing model results

2.5.1 Method of model evaluation

To assess the accuracy of the tracer model, point-to-point comparison between simulated results and existing data are made. Data were collected during four cruises: Polarstern 2007, Wilfried Laurier 2007, GEOTRACES cruises 2009 and 2015 (Table 2.4).

Reference	Year	Location	diss.^{230}Th	tot.^{230}Th
Grenier et al. (in prep.)	2007	Canada Basin	Y	
Valk et al. (in prep.)	2007	Eurasian Basin	Y	Y
Grenier et al. (in prep.)	2009	Canada Basin	Y	
Grenier et al. (in prep.)	2015	Canada Basin	Y	
Valk et al. (in prep.)	2015	Eurasian Basin	Y	

Table 2.4: Data sources for model-data comparisons.

2.5.2 Method of sensitivity analysis

The sensitivity analysis is evaluated on section (a) in Fig. 2.8 to explore unique properties of each run. This section is selected because it connects the Canada Basin to the Alpha Ridge and is a key pathway for high ^{230}Th in the model.

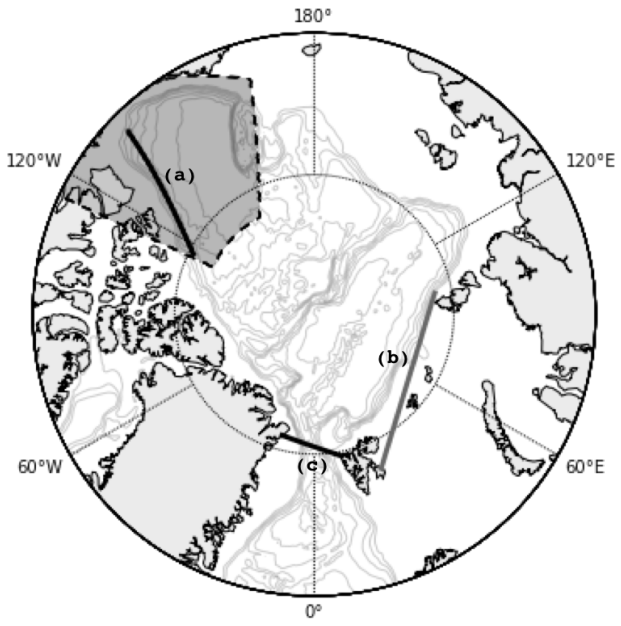

Figure 2.8: Sections involved in sensitivity analysis and physical calculations. The shaded area is the Canada Basin region used for average topostrophy (2.14) and wind stress curl. Section (a) the Alpha Ridge to the Canada Basin is used for tracer analysis; Section (b) Kara and Barents Sea opening and (c) Fram Strait are used for the dense water inflow calculation.

Tracers at approximately 1000 m depth are chosen as representative of the tracer evolution in the intermediate layer. Results are visualized as Hovmoller diagrams to highlight the tracer distribution evolution.

2.5.3 Method of boundary current analysis

In order to visualize model vector flow fields, a scalar field, topostrophy, is employed in diagnosing circulation (Holloway et al., 2007). In the northern hemisphere, positive topostrophy corresponds to flows that tend to keep shallow water to the right. Therefore, positive topostrophy characterizes cyclonic boundary currents in the Arctic, while negative topostrophy represents anticyclonic boundary flows.

The definition of topostrophy ($\mathcal{T}$) is:

$$\mathcal{T} = \vec{\mathcal{U}} \times \nabla\mathcal{H}\ \hat{z} \tag{2.14}$$

where $\vec{\mathcal{U}}$ is yearly mean horizontal velocity, $\nabla\mathcal{H}$ is the gradient of total depth and $\hat{z}$ stands for the unit vertical vector. In order to characterize the change of flow

pattern in the Canada Basin, a sum of topostrophy over Canada Basin is used (Fig. 2.8).

2.5.4 Method of physical component calculations

Calculations of dense water influx

Influx calculation focuses on two main passages: the Barents Sea and Fram Strait (Fig. 2.8). In this study, the dense water influx is the total flux of water denser than $\sigma_\theta = 28.05$, which represents the separation of the Atlantic layer and the deep layer (Lique et al., 2010).

Chapter 3

Results

The first half of this section presents model results and model evaluation. The second half displays comparison analysis between two different dynamics fields (salinity and temperature fields) from EXH001 and EXH005, to understand potential factors that contribute to the different behaviors in the two flow fields.

3.1 Model evolution

3.1.1 Dissolved ^{230}Th

The tracer analysis presented here is at a depth of 1000 m. I chose this depth for two reasons: first, the section of the 2009 ^{230}Th observations that deviates from linearity was centered within the Atlantic Water (Francois and Soon, 2010), from approximately 500-1500 m; second, as mentioned in Section 2.5, the Atlantic layer is defined as a layer between isopycnal $\sigma_\theta = 27.8$ and $\sigma_\theta = 28.05$, with the shallow limit at 200-400 m depth and the deeper limit at approximately 1500 m depth (Lique et al., 2010). Therefore, I assume isopycnal $\sigma_\theta = 28.0$ is a reasonable central location for the core Atlantic layer, which is roughly at depth 1000 m.

Over the time series, the simulated ^{230}Th pattern in the Arctic Ocean experienced a substantial change. The evolution of simulated dissolved ^{230}Th can be separated into four phases: phase I - before the change (2007), phase II - during the change (2009), phase III - shortly after the change (2015) and phase IV - long after the change (2020). Note that the characteristic year for each phase was chosen to match a cruise date for which we have ^{230}Th data: 2007, 2009, 2015.

In phase I, simulated dissolved ^{230}Th showed highest concentrations over the Alpha Ridge and showed lower values in both the Canada and the Eurasian basins (Fig. 3.1 (a)). This spatial pattern is in good agreement with the previous observation patterns, which showed that scavenging intensity was lower in the central Arctic and higher in the Canada Basin and the Eurasian Basin (Edmonds et al., 1998; Scholten et al., 1995). One noticeable feature in this phase is that a low ^{230}Th tongue originating from the low sea ice Canada Basin displayed a northward extension along the Canada Basin side of the Alpha Ridge.

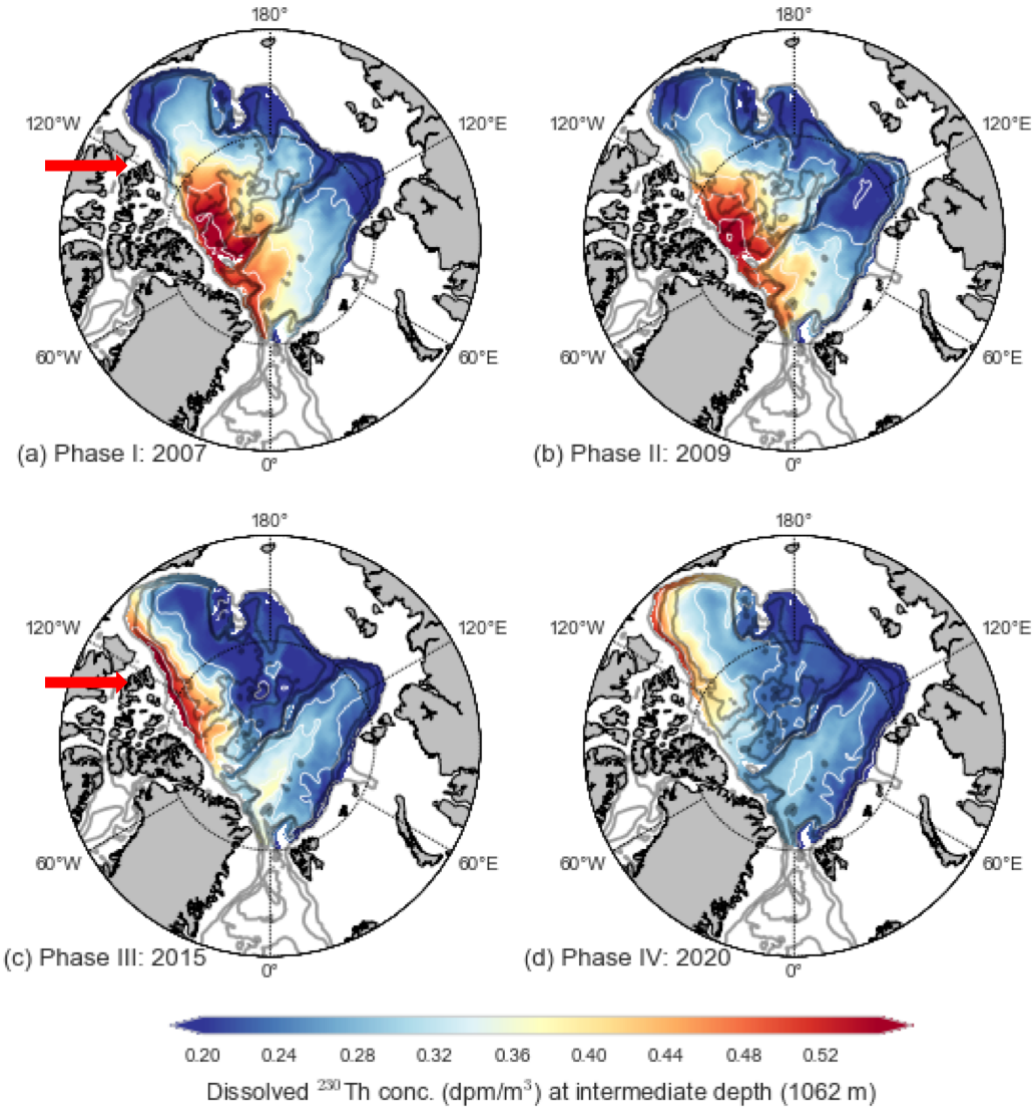

Figure 3.1: Simulated dissolved ^{230}Th concentration in phase (a) I (2007), (b) II (2009), (c) III (2015) and (d) IV (2020). Tracer concentrations shown here are annually averaged model results. In phase I, a low ^{230}Th concentration tongue is seen extending from the Canada Basin (red arrow in (a)). In phase III, a similar tongue but of high ^{230}Th extended from the Alpha Ridge (red arrow in (c)). High concentrations seen in phase I (2007) and phase II (2009) moved southward along the CAA in phase III (2015) and dissipated in phase IV (2020).

In phase II, the overall spatial variation of dissolved ^{230}Th concentrations did not change dramatically compared to phase I. However, there was a small change in

the south Canada Basin - the northward-moving, low ^{230}Th tongue seen in phase I disappeared. Instead, this low ^{230}Th concentration water mass accumulated in the south the Canada Basin.

In phase III, changes in the spatial pattern of dissolved ^{230}Th became more observable. First of all, there was a high ^{230}Th concentration tongue developed with a very pronounced southward progression (Fig. 3.1 (c)). Also, the simulated high ^{230}Th concentration zone was displaced further south toward the Canada Basin, compared to its previous position which had been maintained through phase I and II. Meanwhile, the low ^{230}Th concentration that accumulated in the south Canada Basin in phase II now moved eastward to the Chukchi Plateau side of the Canada Basin.

A notable feature revealed by phase IV (Fig. 3.1 (d)) is that the previously high ^{230}Th concentration water over the Alpha Ridge was completely flushed away and replaced by new, relatively lower ^{230}Th from adjacent water masses. The high ^{230}Th concentration water mass moved further south to the Canada Basin and progressively dissipated during its journey to the south. By phase IV, a transition to a new, remarkably different spatial pattern had been accomplished.

Observations (Francois and Soon, 2010) indicate similar changes - high ^{230}Th values began to invade the Canada Basin in 2007 and were more wide spread in the basin in 2009. However, the modeled tracer evolution in the Canada Basin has a different timing - the emergence of each phase is slightly delayed compared to the observations. Note that although timing does not match well, the model captured the main trends of ^{230}Th evolution. This indicates the model has a similar behavior with observations but it does not reproduce the change at the right time.

3.1.2 Particulate ^{230}Th

Compared to the distribution of dissolved ^{230}Th, the particulate distribution has more spatial and temporal variation (Fig. 3.2).

In phase I, the spatial pattern of particulate ^{230}Th was similar to the dissolved ^{230}Th pattern. There was a low particulate ^{230}Th tongue extending from the south Canada Basin, along the edge of the Canada Basin, to the Alpha Ridge, where the highest particulate ^{230}Th was found (Fig. 3.2 (a)). Unlike the dissolved phase, there were some intermediate concentrations of particulate ^{230}Th at the seasonally ice free edge of the Canada Basin and the Eurasian Basin.

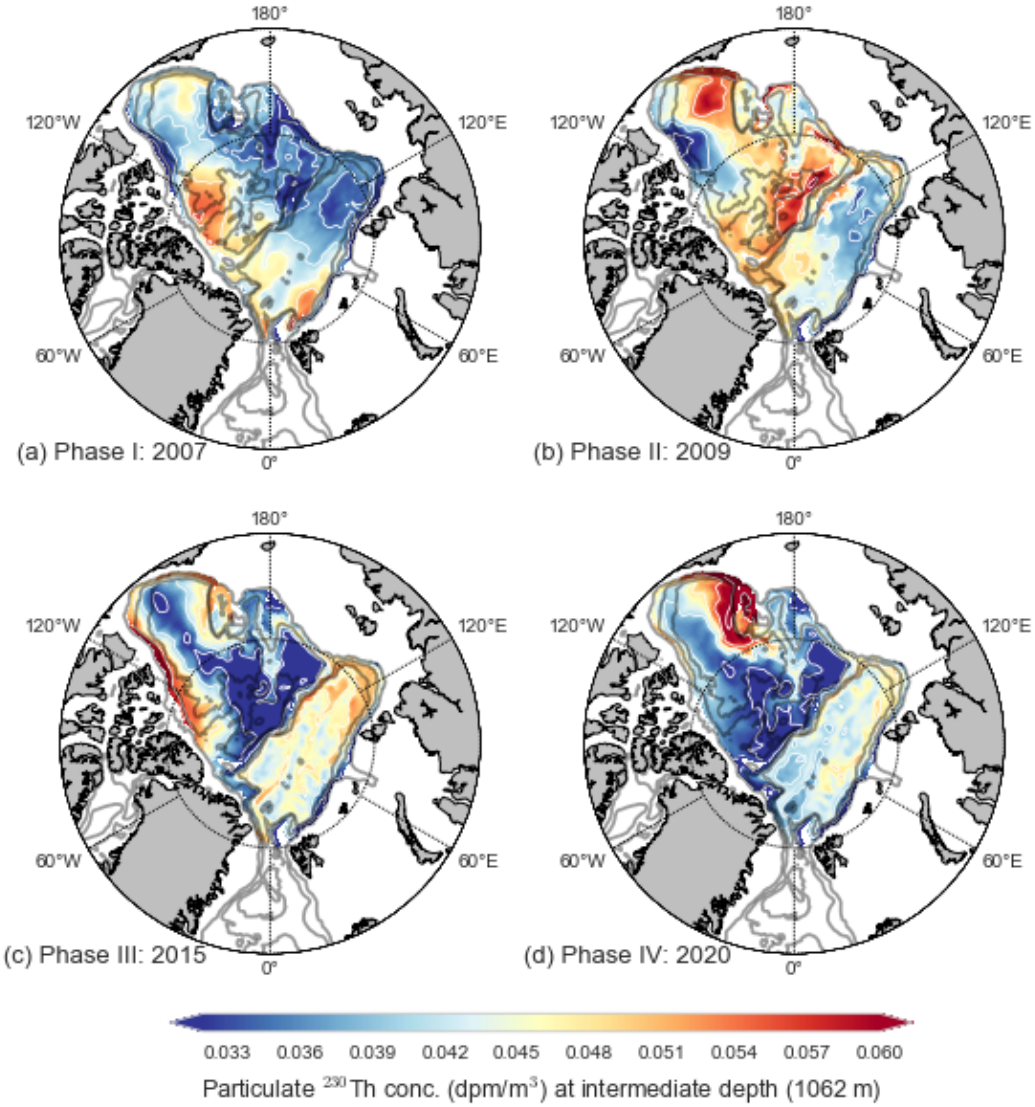

Figure 3.2: Simulated particulate ^{230}Th concentration in phase (a) I (2007), (b) II (2009), (c) III (2015) and (d) IV (2020). Tracer concentrations shown here are annually averaged model results. High concentration seen over the Alpha Ridge in phase I (2007) and II (2009) moved southward along edge of the Canada Basin in phase III (2015) and IV (2020).

Phase II exhibited a domain-wide increase in modeled particulate ^{230}Th (Fig. 3.2 (b)). The largest increases occurred in the Canada Basin and the Makarov Basin. This is associated with the dramatically low sea ice coverage event observed in 2007, when the sea ice coverage was at its 2nd lowest on record. The two-year

(2007-2009) delay in responding to the sea ice is due to the sinking process.

In phase III, as the sea ice concentration slightly rebounded after 2007, the Arctic-wide high particulate ^{230}Th pattern disappeared - the simulated ^{230}Th dropped back to its previous level (Fig. 3.2 (c)). However, the high particulate ^{230}Th concentration over the Alpha Ridge was not maintained. It developed into a narrow tongue that propagated along the northern edge of the Canadian Arctic Archipelago, similar with that seen in the dissolved ^{230}Th.

This high particulate ^{230}Th tongue arrived at the Chukchi plateau side of the Canada Basin in phase IV, with the rest of the Amerasian Basin filled with low particulate ^{230}Th concentration water and the Eurasian Basin occupied with intermediate particulate ^{230}Th concentration water. (Fig. 3.2 (d)).

Unlike the high dissolved ^{230}Th concentration tongue which dissipated along its pathway, the particulate ^{230}Th tongue increased its value during its way southward.

Unfortunately, there is not particulate ^{230}Th data available to evaluate the simulated particulate ^{230}Th evolution over the modeling period. However, judging by the reasonable behavior of simulated dissolved ^{230}Th, one can conclude that although any analysis for simulated particulate ^{230}Th should be undertaken with care, this evolution is reasonable.

3.1.3 Particle field

The particle field is generated by the ice-particle model (2.11) that simulates the movement of advected and sinking particles. Note that the 'particle' field here is not tracking the particle concentration but an ice fraction which has an implicit relation to the particle concentration; this field will be referred to as the 'pseudo-particle field'. Keep in mind that the sea ice fraction and the marine particle concentration are inversely correlated; low/high values of the pseudo-particle field are associated with high/low particle concentrations, respectively.

In phase I, high pseudo-particle values accumulated over the central Arctic region (Fig. 3.3 (a)). Much lower pseudo-particle values were found around the east edge of the Eurasian Basin and the south boundary of the Canada Basin. The low pseudo-particle values in the Canada Basin exhibited a weak northward tongue along the basin boundary.

In phase II, the tongue disappeared along with a significant shrinking in the high pseudo-particle pool (Fig. 3.3 (b)). This Arctic-wide decrease in the pseudo-particle values is coincident with the appearance of Arctic-wide increase in particulate ^{230}Th concentrations. During this shrinking event, there is a newly-formed low pseudo-particle area developed around the Chukchi plateau; this location also documents a transient occurrence of high particulate ^{230}Th zone at the same time (Fig. 3.2).

In phase III, the high pseudo-particle pool went back to its normal size. However, different from previous years, the high pseudo-particle region extended from the Alpha Ridge to the south Canada Basin with the low pseudo-particle water mass

moving toward the Chukchi Plateau side. This spatial pattern remained in phase IV.

Despite the temporal change, there is a robust spatial pattern to the pseudo-particle field - the highest pseudo-particle value (suggesting the lowest particle concentration) always appears north of the Canadian Archipelago, while lowest pseudo-particle value (suggesting the highest particle concentration) is located along the south edge of the Canada Basin and the east edge of the Eurasian Basin. It is also notable that the low pseudo-particle locations have high similarity with the high particulate ^{230}Th zones.

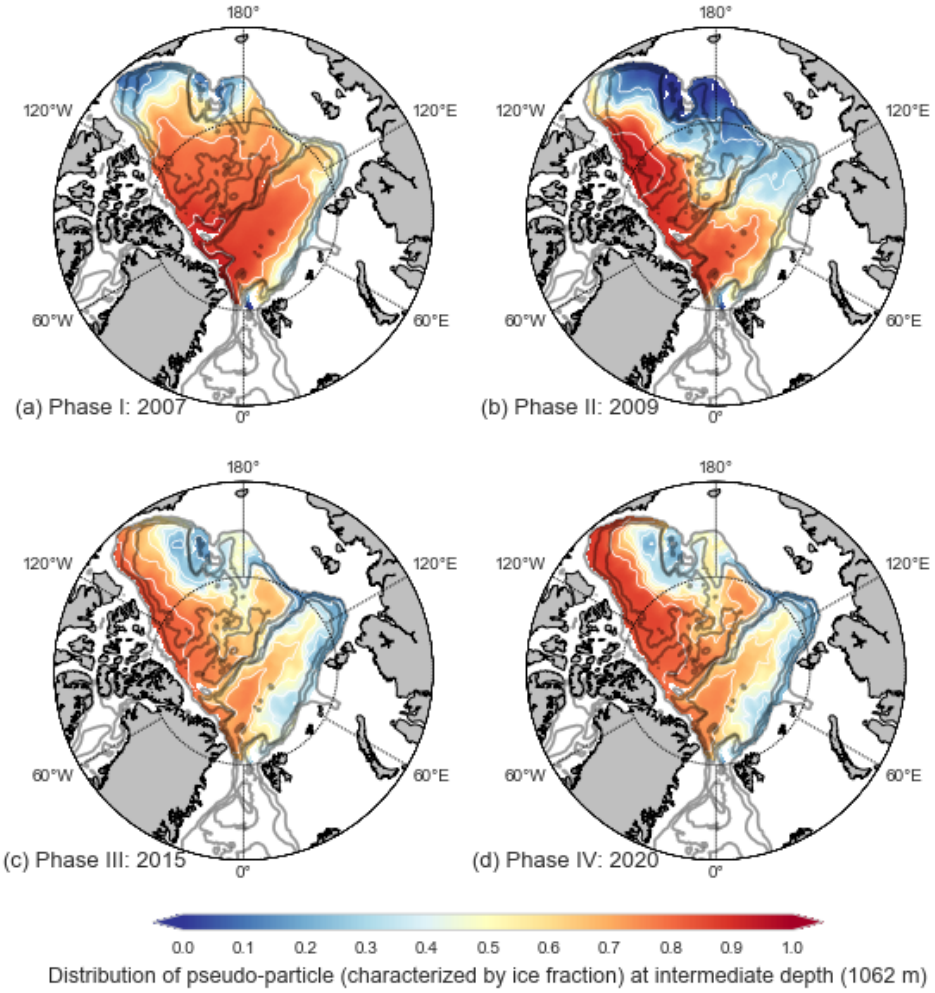

Figure 3.3: Distribution of pseudo-particle in phase (a) I (2007), (b) II (2009), (c) III (2015) and (d) IV (2020). Note that low/high pseudo-particle values are associated with high/low particle concentrations, respectively. The low pseudo-particle locations have high similarity with the high particulate ^{230}Th zones.

3.2 Model evaluation

Canada Basin

To assess model accuracy, a model and data comparison was conducted. The main focus was on the Canada Basin where the temporal coverage of ^{230}Th data was greatest.

As indicated previously, the tracer model has a delay in the change of ^{230}Th concentration in the Canada Basin. To study the lag between the observation and the simulation, time series of ^{230}Th concentration in the south Canada Basin (shaded area in Fig. 3.4) at 1000 m depth are presented. In the model, an increase in thedissolved ^{230}Th concentration started in 2009, reached a maximum in 2015 and the maximum ^{230}Th values decreased slightly since then (Fig. 3.4). In the observations, however, the dramatic increase of ^{230}Th appeared in 2009 instead of 2015. It suggests the modeled change of ^{230}Th concentration in the Canada Basin is six years delayed.

Therefore, in order to have a fair data-model comparison, the model comparison conducted here is evaluating the model behavior at different 'evolution status', rather than directly comparing data with model results in the same sample year. Suggested by the lag, the observed 2009 data was compared with simulated result in phase III (in model year 2015, when the highest simulated ^{230}Th concentration occurred in the Canada Basin). Data from the GEOTRACES cruise in 2015 is compared with phase IV (2020, which is 5 years after phase III).

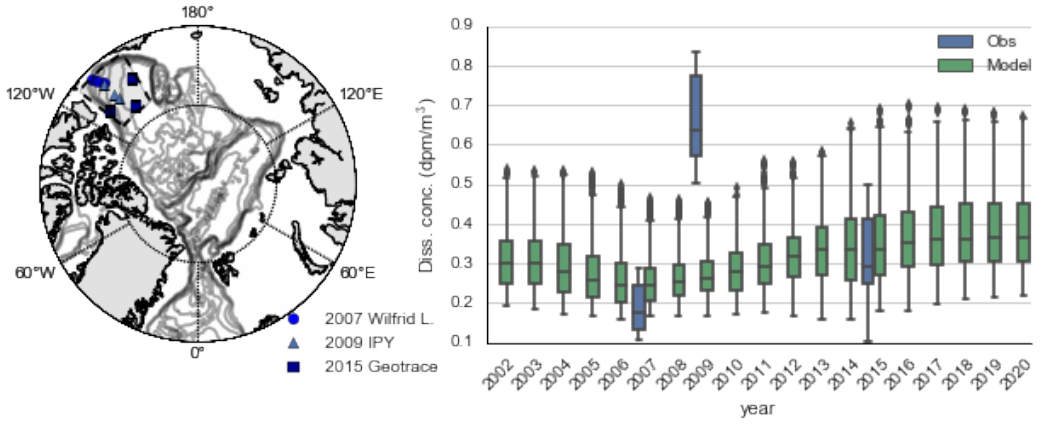

Figure 3.4: Tukey box plots showing modeled and observed time series of dissolved ^{230}Th concentration at between 500-1500 m depth. Each box shows data range from first to third quartile, and median (central horizontal line); black dots show extremes (Tukey, 1977). The green boxes (and black points) represent the simulated ^{230}Th concentrations in the Canada Basin (the shaded area). The blue boxes show the observed data.

The 2007 and 2015 observed ^{230}Th profiles in the Canada Basin are close to but not exactly, straight lines (Fig. 3.5 (a-i)). This shape is captured by the simulated profiles in the Canada Basin, which show an increase with depth. Also, the simulated ^{230}Th magnitudes appear realistic compared to the observations in 2007 and 2015 (Figure 3.5 (a-c, g-i)).) The major deviation from the observations is found in the intermediate layer in 2009, where the model tends to underestimate the ^{230}Th concentration. However, the model predicts reasonable values in the surface and the deep layer.

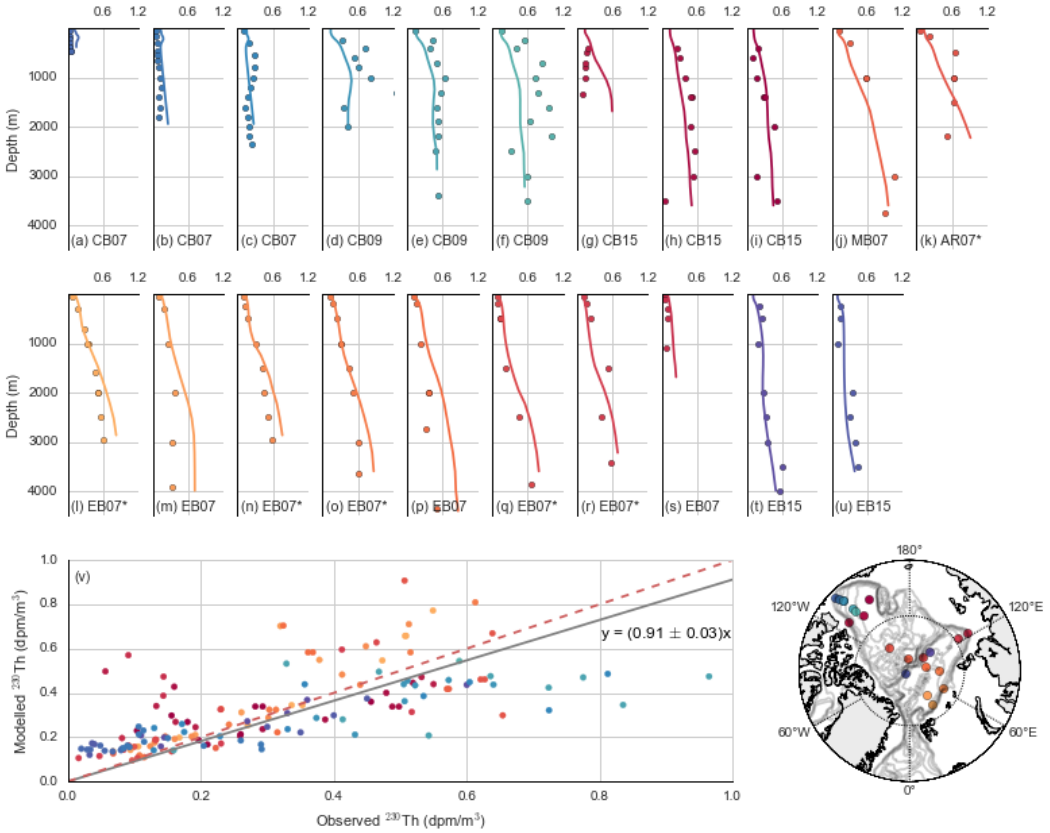

Figure 3.5: Observed versus modeled ^{230}Th. Panels (a-u) show observed ^{230}Th profiles (points) from the Canada Basin, Makarov Basin, Alpha Ridge and the Eurasian Basin versus model results (curves) (*: total ^{230}Th; without *: dissolved ^{230}Th). Sample locations are mapped with different colors. Panel (v) is an linear regression of observations versus simulations. Red dashed line is a reference line showing y=x.

Other basins

In the Eurasian Basin, simulated dissolved ^{230}Th is consistent with observations in both magnitude and vertical structure (Fig. 3.5 (l-u)).

As for the central Arctic (areas above the Alpha Ridge and in the Makarov Basin) that are permanently covered with ice, the observation profiles are not as linear as those in the Canada Basin and Eurasian Basin. More specifically, the values of observed ^{230}Th in the intermediate layer always exceeds (or equals to) the values in the deep layer. As such, while the simulated ^{230}Th in this region appears to be realistic in the surface and deep layers, the simulated ^{230}Th in the intermediate layer is underestimated (Fig. 3.5 (j,k)). For example, at a depth of 1000 m, the average ^{230}Th concentration of the observed data is approximately 0.6 dmp m^{-3} but the model only produces a range of 0.3-0.5 dmp m^{-3}. This reveals that the estimated scavenging intensity in this specific layer is still not low enough in the model.

In order to provide a more quantitative evaluation of the simulation, a linear regression between model and ^{230}Th observations is performed (Fig. 3.5). The result shows large scatter between the model and the observations when the value of observed ^{230}Th is greater than 0.8 dmp m^{-3} and lower than 0.2 dmp m^{-3}. This indicates the model performance is less satisfactory in simulating very high and very low ^{230}Th values.

However, the values of the slope of the linear regression, an indicator to assess the ability of the model in simulating the tracer distribution, gives 0.91 $\pm$ 0.03, a value that is very close to 1. The discrepancy between the reference and the regression is in acceptable range. It reveals that despite the uncertainty in producing very high/low ^{230}Th values, the model, in general, is in good agreement with the observations. This can be supported by the reasonable spatial contrast between the high ice region in the central Arctic and the low sea ice zone in both the Canada and Eurasian basins, and the well simulated vertical structures that are broadly consistent with observations.

3.3 Sensitivity experiments

As the ^{230}Th concentrations are controlled by the scavenging process and the physical process such as advection/diffusion, I conducted two sensitivity experiments (see section 2.4) to test the contribution of each process to understand the change in ^{230}Th concentrations.

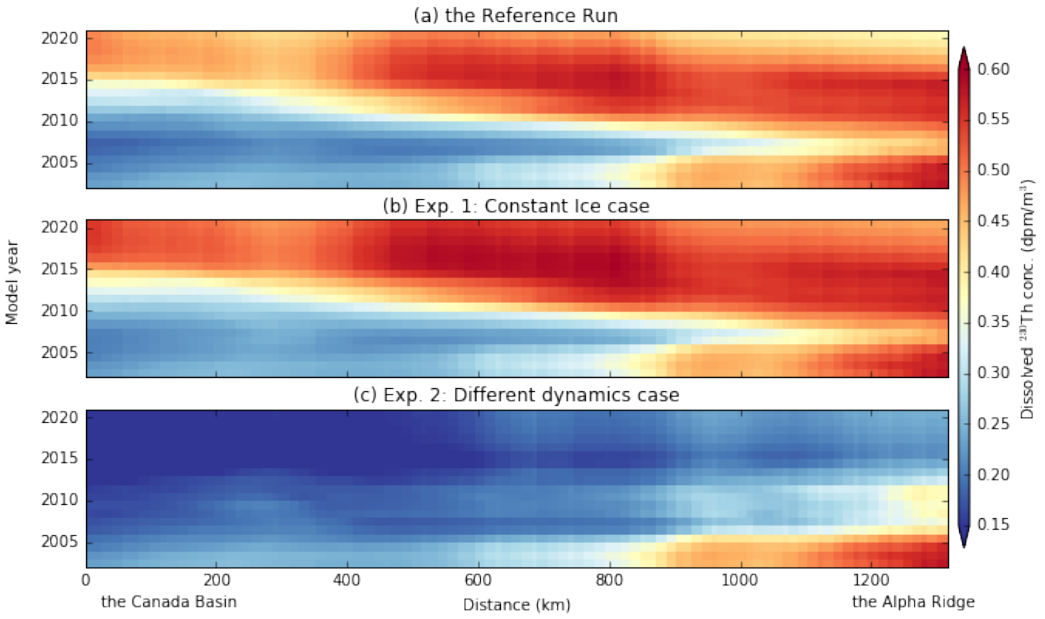

Figure 3.6: Simulated dissolved ^{230}Th concentration at 1000 m depth versus time for (a) reference run and sensitivity experiments (I (b) and II (c)). The left end of this section is to the south in the Canada Basin and the right end extends north to the Alpha Ridge. Run descriptions can be found in section 2.4. Results show that the reference run is similar with Exp. 1 but very different from Exp. 2.

3.3.1 A constant ice case

Dissolved ^{230}Th

The only difference between sensitivity Exp. 1 (Fig. 3.6 (b)) and the reference run (Fig. 3.6 (a)) is the sea ice concentration, which varies annually in the reference run but is held constant at 2002 values in Exp. 1. Experiment results show a high similarity between Exp. 1 and the reference run throughout the model period.

Focusing on a vertical section along the north edge of the CAA (section (a) in Fig. 2.8), we see, in both runs, two distinct water masses. Between 2002 and 2015, the Canada Basin side was occupied with relatively low dissolved ^{230}Th concentration water, while the Alpha Ridge side had much higher ^{230}Th concentrations. In between, water masses from both sides took turns to dominate. From 2002 to 2007, the low ^{230}Th water from the Canada Basin dominated the mid-section. However, starting from approximately 2007, this situation changed - the low ^{230}Th water mass was slowly pushed back toward the Canada Basin by high dissolved ^{230}Th from the Alpha Ridge. By 2015, the whole section was filled with the high ^{230}Th water.

Although these two runs are very similar, a slight difference exists: tracer concentrations from the constant ice case (Exp. 1), were always higher than that of

the reference run. This difference was less obvious in the early part of the run but became more noticeable in time.

Particulate ^{230}Th

For the particulate phase, comparing results for variable ice versus constant ice also shows high similarity in the tracer evolution (Fig. 3.7 (a)(b)).

As in section 3.3.1, we focus on the vertical section north of CAA, where we see it is dominated by a low particulate ^{230}Th water mass from the low ice Canada Basin and a high particulate ^{230}Th water mass from the Alpha Ridge. In both the reference and Exp. 2 runs, the high ^{230}Th labeled water dominated the section shortly after 2007. The similarity in the qualitative behavior between these runs reveals that the ice field has limited effect on the tracer distributions.

It should be noted that, in the reference run with variable ice (Fig. 3.7 (a)), there is a short-term, section-wide increase in particulate ^{230}Th recorded from approximately 2014 - 2015. This occurred 2-3 years after 2012, when sea ice concentration was at record low. The length of this time coincides with that required for the particles to sink from surface to the current depth.

This fluctuation in particulate ^{230}Th, however, is not found in Exp.1, in which the sea ice concentration was the same in each year. These findings indicate that, although the persistent increase in particulate ^{230}Th field that began in 2007 was not caused by the ice, the short-time scale fluctuations were caused by it. This explanation can equally apply to the temporary Arctic-wide increase in particulate ^{230}Th seen in phase II that showed up 2-3 years after 2007 (Fig. 3.2).

3.3.2 A different flow scheme case

Dissolved ^{230}Th

While Exp. 1 tests the tracer sensitivity to changes in sea ice concentration, Exp. 2 tests how sensitive the tracer is in response to changes in the circulation.

Exp. 2 (Fig. 3.6 (c)) produced significantly different results as compared to those of the reference run. Between 2002 and 2007, the dissolved ^{230}Th distribution is similar in the two runs. Low ^{230}Th water occurred on the Canada Basin side and high ^{230}Th labeled water occurred on the Alpha Ridge side. However, after 2007, high ^{230}Th water in the reference run spread southward but the change did not occur in Exp. 2. This experiment suggests that the ^{230}Th distribution is very sensitive to the circulation.

Next, I investigated the velocity fields in the reference run and in Exp. 2 (Fig. 3.8).

In the period 2002 - 2006, a strong northward velocity dominated in the selected section in both runs. This flow transported low ^{230}Th concentrations from the Canada Basin to the Alpha Ridge. A significant change took place in 2007 - ve-

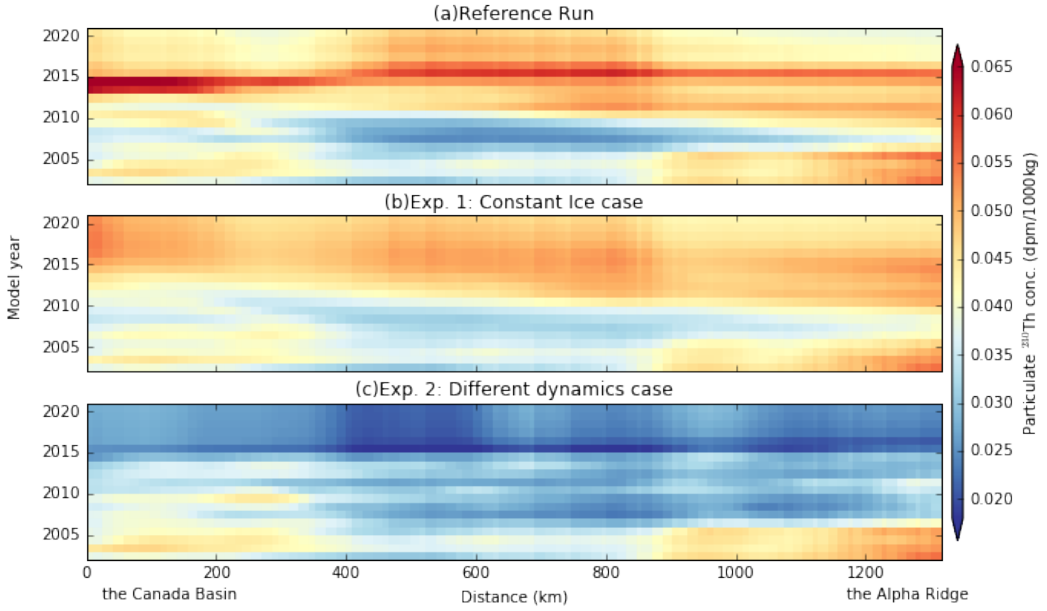

Figure 3.7: Simulated particulate ^{230}Th concentration at 1000 m depth versus time for (a) reference run and sensitivity experiments (I (b) and II (c)). The left end of this section is at south the Canada Basin and the right end extends north to the Alpha Ridge. Runs descriptions can be found in section 2.4. Results show that the reference run is more similar to Exp. 1 than to Exp. 2.

locity direction totally reversed in the reference run; however, the velocity direction in Exp. 2 remained northward. This velocity shift is coincident with the southward propagation of high ^{230}Th labeled water in the reference run. Almost immediately after the circulation pattern switched, the tracer concentrations increased progressively. The high ^{230}Th concentration eventually arrived in the Canada Basin in 2015.

The distance between the Alpha Ridge and the south Canada Basin is approximately 1500 kilometers. With an average southward velocity of 0.006 m s^{-1} in the reference run, the time for high dissolved ^{230}Th arrive at the south Canada Basin is approximately 8 years. This is consistent with the tracer evolution we see in the reference run.

Particulate ^{230}Th

As with dissolved ^{230}Th, results from reference run and Exp. 2 show that the differences between these runs increased after 2007. After 2007, the mid-section of line CAA in the reference run was filled with high particulate ^{230}Th concentration from the Alpha Ridge; however, in Exp. 2 this region had low particulate ^{230}Th from

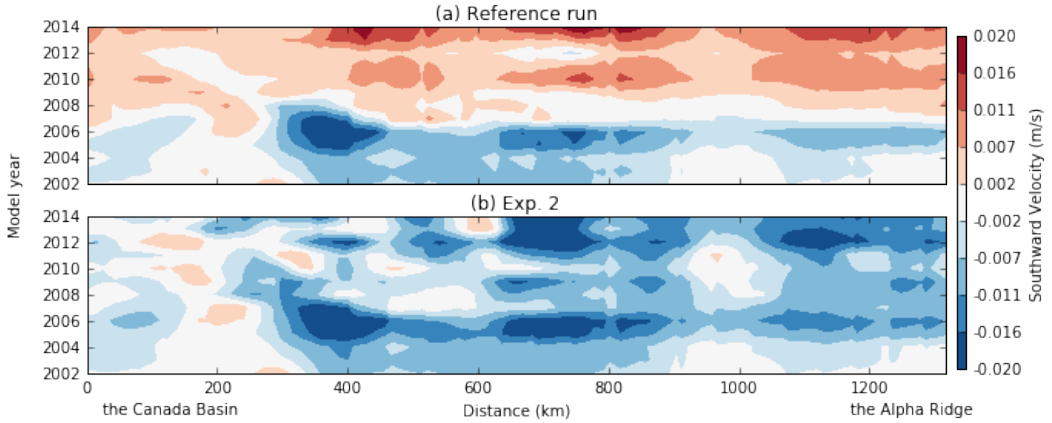

Figure 3.8: Vertical cross-section of along shore velocity along CAA line (section (a) in Fig. 2.8) in (a) reference and (b) Exp. 2. Results show the velocity changed direction in the reference run but not in Exp. 2.

the south Canada Basin. This pattern, similar with that in dissolved ^{230}Th results, suggests particulate ^{230}Th has a rapid response to the circulation (Fig. 3.8)).

Section summary

Exp. 1 indicates the ice-particle field has a more rapid impact on the particulate ^{230}Th than the dissolved ^{230}Th. More importantly, it demonstrates that tracer spatial patterns persist even though the sea ice conditions are different. On the other hand, Exp. 2 demonstrates that the circulation field is crucial in creating the high ^{230}Th zone in the Canada Basin.

As such, the increase in observed and modeled ^{230}Th concentrations in the south Canada Basin suggests an establishment of southward directed currents along the CAA line. As the water transport in the Arctic mainly occurs along the boundaries, the velocity direction along the CAA line implies the general circulation pattern in the Canada Basin. Thus the change of transport direction along the CAA line (from north to south) indicates a general change in the Canada Basin (from cyclonic to anticyclonic).

That engenders a follow-up question: what factor leads to the change in intermediate circulation pattern in the reference run and why did the anticyclonic pattern not show up in Exp. 2?

3.4 Hydrographic comparisons of two flow scenarios

This section provides further analysis on the two different circulation runs. I first investigated the topostrophy evolution during the model period, then explored hydrography differences in the runs along the boundary of the Arctic Ocean.

The years chosen to display here are different from those in the tracer analysis. As revealed by the simulated ^{230}Th, the flow pattern in the reference run started to change during 2007. As a result, I selected 2006, 2007, 2008 to investigate the transition of the flow field. For a comparison purpose, analysis in Exp. 2 also contains these years, even though the change is not seen in this run.

3.4.1 Topostrophy analysis

As mentioned before, isopycnal $\sigma_\theta = 27.8$ and $\sigma_\theta = 28.05$ are the upper and lower bounds for the Atlantic layer. Therefore, isopycnal $\sigma_\theta = 28.0$, centered in between isopycnal $\sigma_\theta = 27.8$ and $\sigma_\theta = 28.05$, is considered as a representative depth for analyzing the flow pattern in the Atlantic layer. I conducted a topostrophy analysis for this layer as a means of comparing the model circulations.

The results show that, in 2006 (before the change), the topostrophy fields along the isopycnal $\sigma_\theta = 28.0$ are similar in the reference run and Exp. 2 (Fig. 3.9). In this year, positive topostrophy dominates over the whole Arctic.

As mentioned in Chapter 2.5.3, positive and negative topostrophy characterizes cyclonic and anticyclonic boundary currents, respectively. This positive topostrophy thus shows that, after the Atlantic water enters the Arctic system through the east side of Fram Strait, it flows in a cyclonic direction in the Eurasian Basin. Part of the water splits from the main loop shortly after it passes the Laptev shelf and enters the Amerasian Basin. After that, this branch flows into the Canada Basin, via the Makarov Basin and the slope of the Chukchi Sea. This pattern can be revealed by a cyclonic transport of low ^{230}Th (in both dissolved and particulate form) along the Arctic boundary in phase I .

During 2007 in the reference run, most of the topostrophy along the boundary of the Amerasian Basin changed from positive to negative. This reversal in the signs of topostrophy field shows the water masses in the Amerasian Basin were in transition from a cyclonic rotation to an anticyclonic rotation. This flow pattern is in contrast to the dominant pattern in the early years and it leads to the transport of high ^{230}Th concentration water from the Alpha Ridge to the south Canada Basin in the reference run, with arrival in 2015.

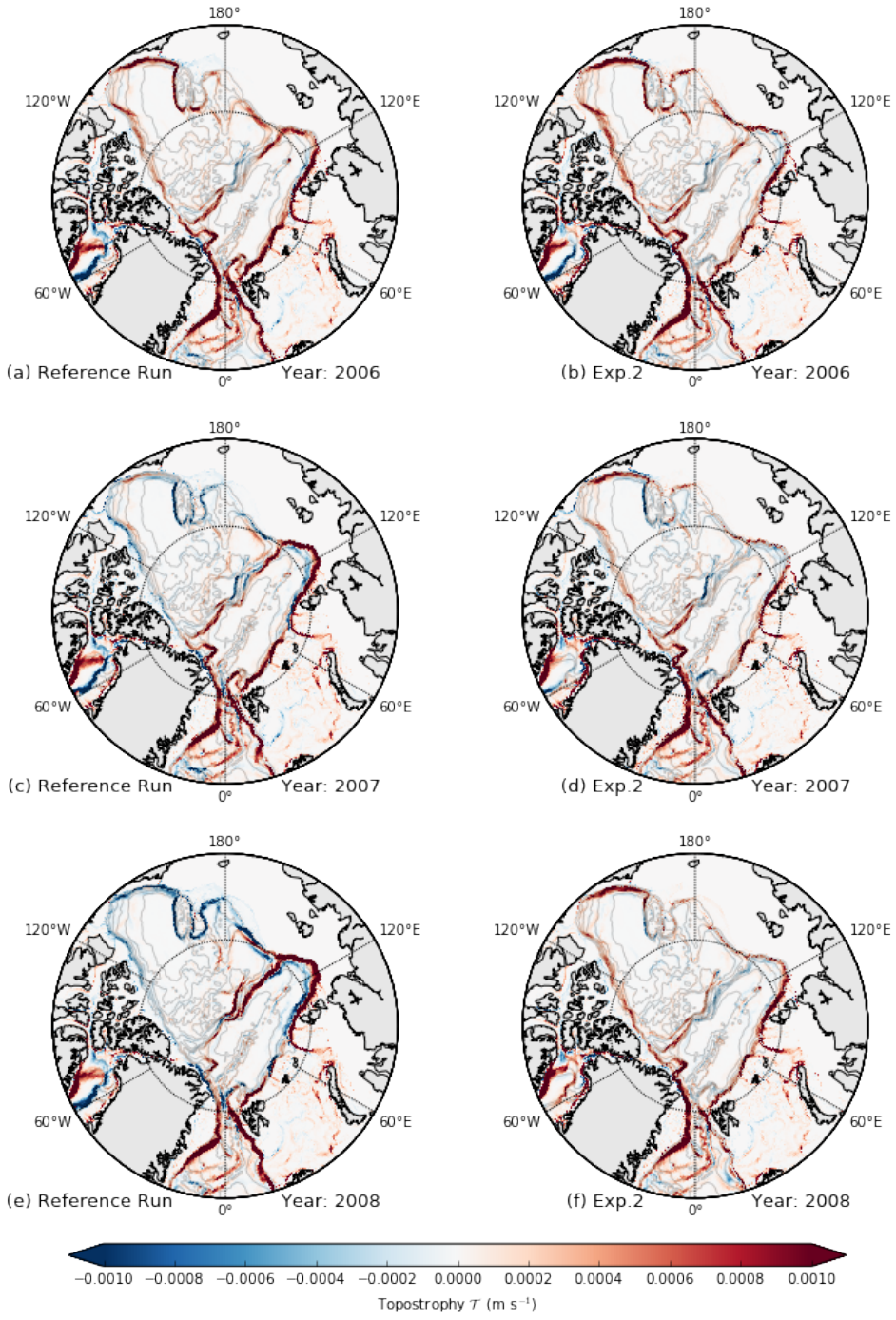

Figure 3.9: Topostrophy along isopycnal $\sigma_\theta = 28.0$ in the reference run and Exp. 2, suggesting significant change in the flow pattern is seen in the reference run but not in Exp. 2.

However, while negative topostrophy occupied most of the Amerasian Basin in the reference run, only a small area with negative topostrophy was found in Exp. 2, around the Chukchi Plateau. It indicates the development of anticyclonic flow in Exp. 2 preliminarily started from the east side of the Amerasian Basin. This negative area in Exp. 2 is coincident with the region with the strongest negative topostrophy signal in the reference run.

The reference run shows that shortly after 2007, the positive topostrophy in the Canada Basin completely disappeared. The negative topostrophy extended farther towards the Alpha Ridge, which indicates the weak anticyclonic flow in the previous year further developed into an Amerasian-basin-wide anticyclonic flow. Also, this anticyclonic flow was intensified compared to 2007, as revealed by more negative topostrophy values in this region. A notable feature is that the absolute values of negative topostropy decreased along the Amerasian boundary, from the east to the west.

However, while the anticyclonic flow was fully developed in the Amerasian Basin in the reference run, the situation in Exp. 2 was quite different. The results show a stronger positive topostrophy signal in the Amerasian Basin, which means the boundary current not only remained cyclonic but was enhanced. Meanwhile, the 2007 small negative signal close to the Chukchi plateau vanished.

3.4.2 Density analysis

In order to understand the hydrographic distributions within the model domain, density variations in 2006, 2007 and 2008 at 1000 m depth, the same depth as used for the tracer analysis, are investigated.

Result shows that the density spatial distribution are similar in both runs in 2006 (Fig. 3.10). Less dense water occurred on the Russia side of the Eurasian and Makarov Basin, with much denser water existing in the central Arctic and around the edge of the Barents Sea.

In 2007, when the topostrophy in the Amerasian Basin reversed sign in the reference run, the boundary current along the Barents and Kara Sea exhibited higher density in both runs. However, compared to the reference run, the increase of density was less obvious in the Exp. 2 - its high density terminated at the Laptev side of the Eurasian Basin.

In contrast, the increasing density signal in the reference run spread cyclonically all the way from the Eurasian Basin to the CAA side of the Canada Basin, although the signal dissipated along its pathway.

In 2008, despite the enhanced anticyclonic flow revealed by the negative topostrophy from the reference run (Fig. 3.9), this high isopycnal signal propagated cyclonically around the Arctic. An noticeable feature is that this high density signal was trapped by the shelf slope and always kept the shelf to its right. Also note that its propagation speed was, clearly, much faster than the simulated ^{230}Th signal. These features point to an existence of an internal Kelvin wave.

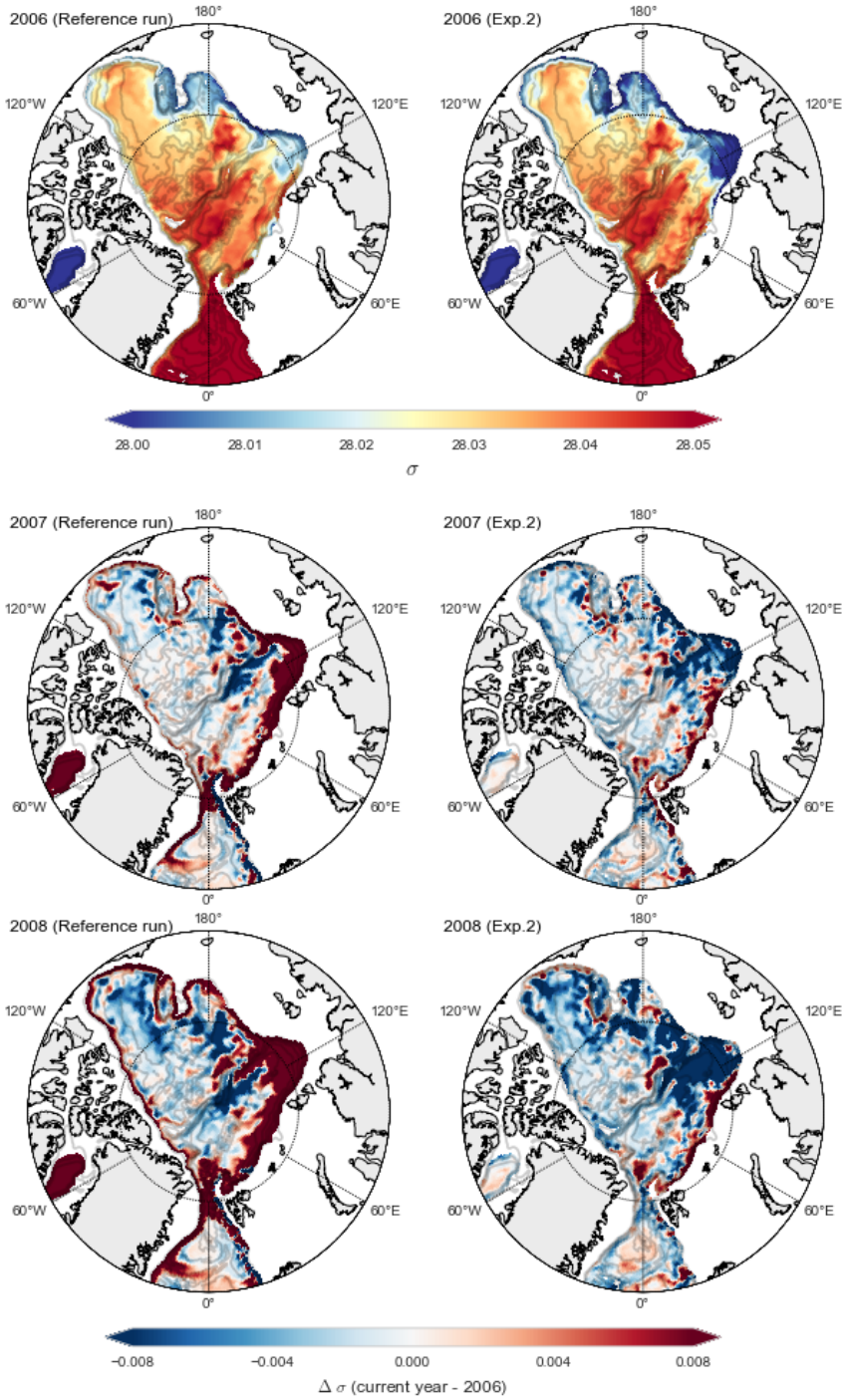

Figure 3.10: Analysis of density variations at 1000 m depth for 2006, 2007 and 2008 for the reference run and Exp. 2. The upper panels show density fields for 2006. The lower panels show the density differences in 2007 and 2008, as compared to 2006, indicating a denser boundary current in the Amerasian Basin in the reference run but not in Exp. 2.

To further study of the propagation of the dense water, an investigation of the core Atlantic layer (isopycnals $\sigma_\theta = 28.0$) in the Amerasian Basin was conducted on the reference run.

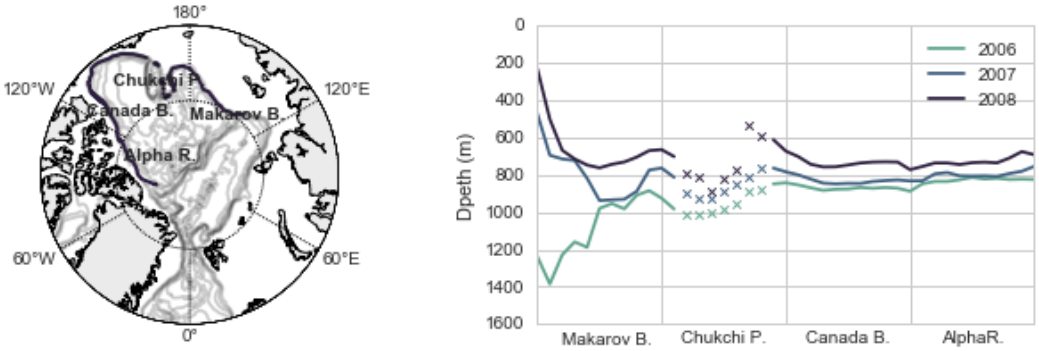

Figure 3.11: The vertical distribution of isopycnal $\sigma_\theta = 28.0$ in the reference run along the 1000 m isobath around the Arctic boundary. The left panel maps the location of the 1000 m isobath. The right panel shows time evolution of isopycnal $\sigma_\theta = 28.0$ in the Amerasian Basin along the Arctic boundary (displayed the map). As the bathymetry around the Chukchi Plateau is complicated to contour, the vertical position of isopycnal $\sigma_\theta = 28.0$ in this region is dotted. Result shows the isopycnal rose in 2007 in the Makarov Basin. The signal reached all the way to the Alpha Ridge, although in diminished amplitude.

Following the isopycnal $\sigma_\theta = 28.0$ (the core layer of Atlantic water), we can see that the depth of this isopycnal σ_θ at the Makarov Basin changed dramatically from 1300 m to 500 m during 2006 - 2007. The density contrast created a wedge-shape isopycnal in the Makarov Basin.

The isopycnal $\sigma_\theta = 28.0$ in the rest of the basin responded accordingly - it was lifted by approximately 50 m at the west side of the Amerasian Basin (the Canada Basin plus the Alpha Ridge) in no more than one year. The timing of this event is coincident with the time when topostrophy reversed signs in the Amerasian Basin (Fig. 3.9).

As flow at this time scale is geostrophic, it is not a surprise that the change in Atlantic isopycnal shape is synchronous with the change in the circulation. The lift of the isopycnals implies the density increased at the continental slope, which implies vertical shear of the boundary current by the thermal wind relationship. This vertical shear implies a more anticyclonic flow in the intermediate layer compared to the deep layer.

In 2008, the isopycnal $\sigma_\theta = 28.0$ in the Makarov Basin was pushed further up. The wedge-shape isopycnal remained in the Makarov Basin. In this year, the isopycnal $\sigma_\theta = 28.0$ in the rest of the basin was lifted another 50 m. Note that previous density analysis indicates while the density along the Arctic boundary

increased after 2007, that in the interior basin decreased (Fig. 3.10). Therefore, the further lifting of isopycnal $\sigma_\theta = 28.0$ means that density contrast between the boundary and the internal ocean were further increased, which created an enhanced anticyclonic flow as implied by the topostrophy field.

The density and the isopycnal analysis suggests that the major difference between the reference run and Exp. 2 is whether the dense water succeeds in penetrating into the deep Arctic and reshaping the isopycnals. When a dramatic lift of isopycnal slope developed along the Arctic boundary (the reference run), one can expect an anticyclonic flow; however, if the dramatic lift of isopycnal slope is not developed (Exp. 2), the anticyclonic flow will not be generated.

3.4.3 The Arctic inflow analysis

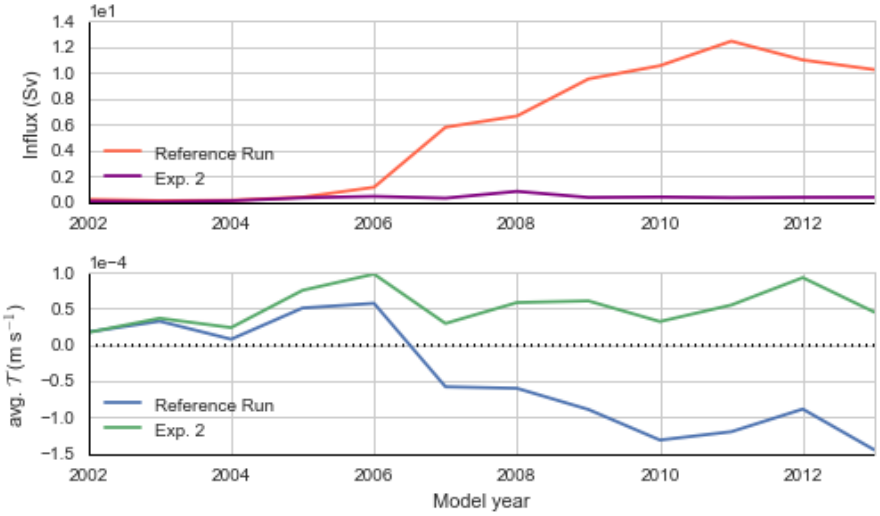

Figure 3.12: The amount of dense water inflows ($\sigma_\theta > 28.05$, from the Barents Sea and the Fram Strait) (upper panel) and average topostrophy in the Canada Basin (lower panel) versus time in both the reference run and Exp. 2, indicating an increase dense water inflow is coincident with a change of topostrophy.

In order to change the shape of the Atlantic layer, there must be a sufficient inflow of dense water. I integrated all inflows where $\sigma_\theta > 28.05$ from a section across the Fram Strait and a section along the Barents Sea shelf (Fig. 2.8; sections b and c, respectively) to further complete the puzzle.

In the reference run, the dense inflow started to increase in 2005 (Fig. 3.12). This moderate increase was followed by a dramatic increase starting in 2006. The highest influx occurred in 2011 with a slightly decrease in the following years.

During this period, topostrophy in the Canada Basin (Fig. 3.12 (a)) persistently

decreased in the reference run. It changed from positive to negative in 2007, which indicated the change from the cyclonic to the anticyclonic circulation pattern.

On the contrary, Exp. 2 maintained a positive topostrophy in the Canada Basin during the model period. Note that its dense water inflow did not dramatically increase as that in the reference run.

While the influence from dense water inflow has been highlighted, its source is left to be determined. There are two branches of inflow that can bring dense water into the Arctic, one is the Fram Strait branch and the other is the Barents Sea branch.

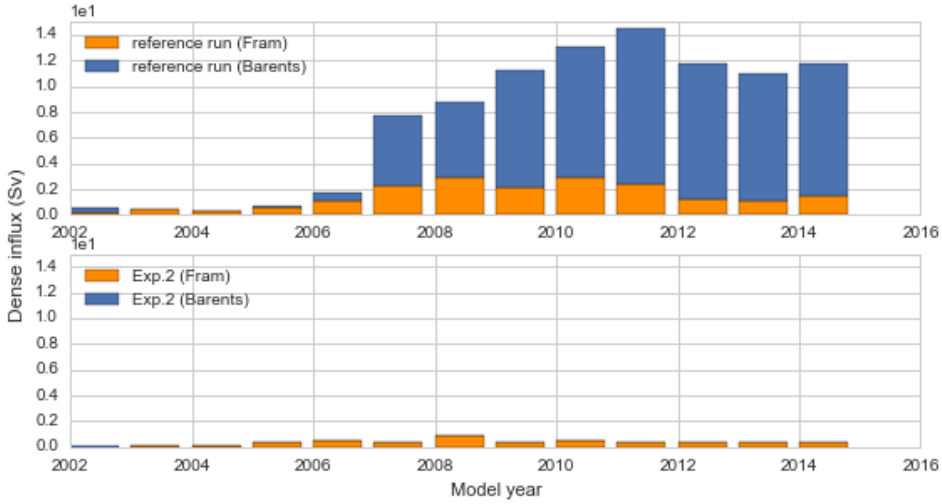

Figure 3.13: Time series of dense water inflow (below $\sigma_\theta = 28.05$ from a section across the Fram Strait and a section along the Barents Sea shelf (Fig. 2.8)) in the reference run (upper panel) and the Exp. 2 run (lower panel). Results suggest the dense water influx that significantly increased after 2006 in the reference run mainly comes from the Barents Sea. However, such change did not appear in Exp. 2.

The increase in the dense water inflow in the reference run starting in 2006 was mainly caused by a significant increase in the amount of Barents Sea dense water. Before that, the dense water was mainly from the Fram Strait. However, the dense water source in Exp. 2 continued to come mainly through the Fram Strait from the Atlantic Ocean (Fig. 3.13). It can be concluded that the difference between two runs is attributed to the increase of dense water input from the Barents Sea.

Finally, there is one last question left to be solved. Despite the differences in the long term linear trend in topostrophy, one may notice that the short term topostrophy variations in both runs are similar. Why is that? Given the fact that both runs are forced by the same wind field, I further investigated the correlation between the wind field and the change of topostrophy.

The wind pattern over the Canada Basin (Fig. 3.14) is anticyclonic due to the

Figure 3.14: Time derivatives of averaged topostrophy over the Canada Basin versus the time series of averaged wind curl over the Canada Basin. Upper panel: the reference run, lower panel: Exp. 2. The wind affects the topostrophy on an annual time scale.

Beaufort high. The time derivative of topostrophy is well correlated with the wind series. The strongest anticyclonic wind was seen in 2007, when topostrophy had large drops in both runs. The second largest decrease occurred almost at the end of runs, 2013, when topostrophy was observed to have a similar downward trend. The topostrophy responds to the wind curl in less than one year.

Chapter 4

Discussion

4.1 Cause of observed increase in ^{230}Th in the Canada Basin

4.1.1 Model Evaluation

The data-model comparison supports the results of the tracer simulation in three ways. First, the general vertical structure simulated by the model is in good agreement with observations. Second, the contrast between the low ice areas and high ice areas is reasonably reproduced. Third, similar to the observations, the simulated ^{230}Th experienced an increase in the Canada Basin in the reference case.

However, there are two main discrepancies between model and data.

First, there is a 6 year difference in the arrival time of high ^{230}Th concentration in the Canada Basin between the observation and simulation. This delay in the change of the simulated tracer is caused by a late change of the velocity pattern in the reference run, suggested by the sensitivity experiments. One can expect the arrival time of high ^{230}Th concentration will get closer to the observation if the change of circulation pattern occurs earlier. Due to the difficulty in accurately modeling all features of the Arctic circulation, I cannot expect to generate an accurate map of ^{230}Th in this study: rather this attempt is a means to answer what circulation changes could have altered the ^{230}Th distribution in the real world.

Second, there is a major dissolved ^{230}Th deviation from the observations found over the Alpha Ridge and in the Makarov Basin region. The model consistently underestimated the tracer concentration in this region, which suggest an overestimation of scavenging intensity over the Alpha Ridge (more discussion in Section 4.3). In this model, the high ^{230}Th concentration over the Alpha Ridge is the main contributor to the high ^{230}Th observed in the Canada Basin. Therefore, the underestimation of scavenging coefficients over the Alpha Ridge directly causes the underestimation of the increase of simulated ^{230}Th concentration in the Canada Basin.

4.1.2 Sensitivity to sea ice concentration

Exp. 1 indicates that the temporal change of sea ice concentration will result in a subsequent change in ^{230}Th concentration by altering the scavenging intensity. Between the two phases of ^{230}Th, the particulate form responds to the sea ice

change more rapidly. In both phases, the difference between the Exp. 1 and the reference run grows slowly in time, suggesting the scavenging adjustment occurs on a relatively long time scale. However, the variation of sea ice accounts for a less than 0.05 dpm m^{-3} variation in simulated ^{230}Th concentration at intermediate depth. Since the overall change at the same depth is more than 0.3 dpm m^{-3}, this experiment indicates that the change in sea ice concentration over the model period is not sufficient to cause the observed change in ^{230}Th concentration.

However, one should keep in mind that this result does not mean sea ice concentration is not important. On the contrary, the spatial pattern of sea ice concentration plays an extremely important role in controlling the distribution of ^{230}Th - because a concentration contrast between the Canada Basin and the Alpha Ridge is required to cause the observed change.

4.1.3 Sensitivity to circulation pattern

Comparison between runs with the same ice concentration but different circulations shows that the change in observed ^{230}Th concentration is directly caused by the shift in circulation. This result is consistent with findings that non-linear profiles of ^{230}Th in the Arctic are generally due to lateral transport (Roy-Barman, 2009).

This change in circulation also leads to a decrease of ^{230}Th concentration over the Alpha Ridge, in addition to the observed increase in the Canada Basin. However, it does not result in a significant change in the Eurasian Basin.

The decreasing tracer concentration over the Alpha Ridge suggests that the build-up of high concentration over the Alpha Ridge requires both low scavenging rates and limited exchange. It leads to a new implication, if the intermediate pattern remains anticyclonic in the Amerasian Basin, the high concentration will not occur again, because the high concentration source cannot be rebuilt. However, if the flow becomes cyclonic again, a high concentration in the Canada Basin might occur next time the anticyclonic flow re-establish, provided high ^{230}Th concentration can rebuild in the high ice region over the Alpha Ridge (at a time scale of a few decades according to a one-dimensional scavenging model - Appendix B.1).

Another important implication from this tracer simulation is that the real-world transition from cyclonic to anticyclonic pattern is stronger than that shown in the model. Assuming the intermediate circulation pattern changed in 2004, as suggested by Karcher et al. (2012), the observed peak of high ^{230}Th concentration arrived in the Canada Basin 5 years afterward. In this study, the circulation pattern shifted during 2007 and the simulated high ^{230}Th peak arrived 8 years later. In the simulation, the newly-formed anticyclonic circulation was weak from 2007 to 2010. It increased progressively and slowly gained speed over 2010. However, judging by the arrival time of observed high ^{230}Th concentration, one can infer that the anticyclonic flow in the real world is different from the simulation - it could be 1.6x stronger, which is quite possible due to the grid resolution (>10 km) versus Rossby deformation radius (∼6 km) (more discussion in Section 4.2).

The modeled arrival of simulated high ^{230}Th is consistent with the modeled velocity. The distance between the Canada Basin and the Alpha Ridge is approximately 1500 kilometers, which, given 5 years, implies a mean real world anticyclonic velocity is of around 0.01 ms^{-1}, compared to the modeled velocity of 0.006 ms^{-1}.

4.1.4 General circulation pattern revealed by ^{230}Th

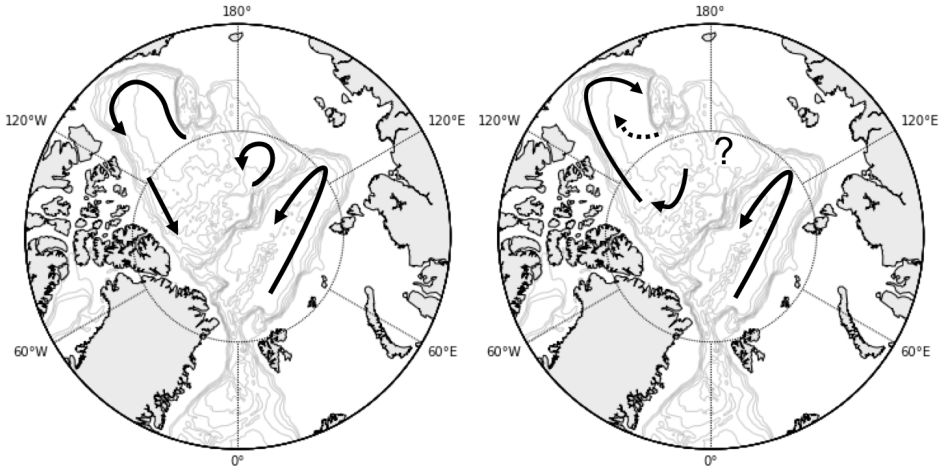

Figure 4.1: Sketch of general circulation pattern (a) before 2007, (b) after 2007 at the intermediate layer (between $\sigma_\theta = 27.8$ and $\sigma_\theta = 28.05$) inferred from simulated ^{230}Th. The flow pattern in the Eurasian Basin remains cyclonic while that in the Canada Basin changed to anticyclonic.

The evolution of ^{230}Th revealed that there are two circulation patterns during the model period (Fig. 4.1). The first circulation pattern contains three cyclonic gyres: in the Eurasian, Makarov and the Canada basins. This is consistent with previous knowledge of the Arctic circulation (Rudels et al., 1994). The second circulation pattern also has cyclonic flow in the Eurasian Basin, however, it has a completely reversed circulation pattern in the Canada Basin. Previous research suggested a small anticyclonic recirculation cell in the Beaufort sea in an overall cyclonic intermediate circulation in the Amerasian Basin (McLaughlin et al., 2009). However, the simulated tracer distribution indicates the switch to an anticyclonic flow is more than a regional phenomenon in the Beaufort sea but, actually, an entire reversal in the Amerasian basin (Fig. 4.1). Otherwise, with just a small anticyclonic region in the Canada Basin, it is impossible for the high concentration ^{230}Th from the Alpha ridge to reach the Canada Basin. Note that this larger scale change not only exists in the model, it is also supported by the real-world ^{230}Th data.

The topostrophy (Fig. 3.9) indicates two counter rotating flows in the Makarov Basin, with the outer flow cyclonic and the inner flow anticyclonic. Unfortunately,

the simulated ^{230}Th distribution in the Makarov Basin does not have enough contrast to reflect these flows.

One feature of the simulation that can be further investigated is the persistence of the anticyclonic flow. In this study, the run is not long enough to track whether the anticyclonic circulation is enhanced in time or weakens or disappears.

4.2 Cause of circulation pattern change

While the tracer model and the tracer observations both confirm the change in circulation, the model uncertainty in timing is not sufficient to conclude when the change happened. However, the combination of two physical flow fields provides a perspective on the mechanism of such change. This study proposes that the change in circulation regime during the mid 2000s was associated with a strengthening of the Arctic dense water inflow (mainly from the Barents Seas).

Effect from wind

This attribution of the change is different from a previous finding that suggested that strong Ekman pumping was the reason for anti-cyclonic intermediate flow (Karcher et al., 2012). Their conclusion came from a strong anticyclonic wind pattern in 2004 that was coincident with the year when the Atlantic layer shifted flow direction. In both my physical runs (the reference run and Exp. 2), a strong anti-cyclonic wind pattern dominated in model year 2007 (Fig. 3.14). Coincidentally, the change of flow pattern in the reference run also showed up at this year.

However, disagreement arises when considering Exp. 2, which is forced by the same wind field as the reference run and therefore also experienced strong anti-cyclonic winds in 2007, did not exhibit an anti-cyclonic circulation.

This study recognizes that wind has an impact on the topostrophy variation in the intermediate layer by compressing intermediate flow at the continental slope but does not agree that the wind is the dominant reason for anticyclonic flow in the intermediate layer. Judging by the response to the wind field in Exp. 2, the response happens at a relatively short temporal scale on the order of a year (Fig. 3.14) and once the anti-cyclonic wind pattern weakens, a rebound in topostrophy is seen immediately.

Effect from dense inflow

Analysis on different flow fields suggests that the change in topostrophy is affected by both a short term effect from the wind patterns (Fig. 3.14) and a long term effect from the variation of dense Arctic inflow (Fig. 3.12). This result is consistent with a previous study that concluded that the intensity of remote inflow and intensity of the surface circulation were the main factors that affected the strength of the circulation in the Atlantic water (Lique et al., 2015). However, since the change in

wind pattern that governs the surface flow is not sufficient to cause the reversal of the flow pattern, my work emphasizes the importance of 'remote forcing'.

In the reference run, the long term linearly decreasing trend in topostrophy is well correlated to a large volume of dense water transported into the Arctic system. This correlation suggests that the dense water input is a necessary condition for anticyclonic movement in the intermediate layer in the Canada Basin. This finding is in agreement with an earlier finding that recognized the importance of dense shelf water in terms of explaining the temperature and salinity characteristics observed in the Canadian Basin (Rudels et al., 1994).

This study suggests that a possible mechanism responsible for the circulation change is a high density wedge that develops and forms an internal Kelvin wave after the dense water inflow alters the previous density distribution. This deduction comes from two reasons: First, the propagation of high density values (or 'signals') is trapped along the continental slope; and despite the anticyclonic movement in the intermediate flow, which has the coastline on its left, the density signal propagates consistently with the coast on its right. Second, the propagation of the density signal is much faster than the model velocity. The average boundary velocity speed in the reference run at 1000 m depth is 0.006-0.008 m s^{-1}. Ignoring the transport in the Eurasian Basin, the distance along the boundary of the Amerasian Basin alone is more than 3000 km. It would take more than ten years for the density signal to advect. However, this signal propagated throughout the Arctic in no more than one year (Fig. 3.10 and Fig. 3.11). This is only possible for a wave, not advection.

The internal Kelvin wave velocity for a two-layer fluid is (eg. Støylen and Fer (2014)):

$$c = \sqrt{\frac{\rho_2 - \rho_1}{\rho_2} g \frac{H_1 H_2}{H_1 + H_2}} \tag{4.1}$$

where ρ_2 and ρ_1 are the density in the upper and lower layer; H_1 and H_2 are the upper and lower layer thicknesses, respectively. Assuming ρ_1 and ρ_2 are 1028.0 kg m^{-3} and 1028.1 kg m^{-3} , and H_1 and H_2 are 1000 m and 2000 m, the propagation of the internal Kelvin wave is 25000 km y^{-1}. In that case, it is not surprising that the isopycnal signal can circle the Amerasian Basin in just one year. This result conforms to previous study that suggests the circulation in the AW layers can adjust to any change of forcing through the propagation of boundary trapped waves (Lique et al., 2015).

The Rossby radius of deformation (R) is:

$$R = \frac{c}{f} \tag{4.2}$$

where c is the wave speed and f is the Coriolis frequency. With $f = 2\Omega \sin(90°)$

($\sim 1.458 \times 10^{-4}$), the Rossby radius is approximately 6 km. As the grid resolution (>10 km) is approximately 1.6x larger than the Rossby radius, it is likely that the wave is only marginally resolved and thus explains why the model velocity was slower than the realistic one that suggested by ^{230}Th observations.

Source of the dense water inflow

The dense water mainly comes from the Barents Sea (Fig. 3.13). The formation of dense Barents Sea Water is facilitated by brine rejection due to ice formation. Due to the dramatic changes in sea ice conditions, the salinity of Barents Sea water has increased over the last 30 years (Oziel et al., 2016; Skogseth et al., 2005).

The highest-ever recorded bottom salinity, 35.83, was observed in 2002 in the deepest pool of Storfjorden (north-west Barents Sea) (Skogseth et al., 2005). To the north of Severnaya Zemlya (between the Barents Sea and the Kara Sea), a very saline and dense bottom layer was also observed in 2007 (Rudels et al., 2013). These observations all imply that the inflow into the Arctic Ocean is becoming denser and thus it is possible that the dense water source has increased.

This argument is also supported by a recent modeling study that finds a 1.5x increase of salt flux under a warming climate, which leads to a threefold increase of shelf-slope volume flux below the warm core of Atlantic water (Ivanov and Watanabe, 2013).

The timing of these increases in density agrees with the ^{230}Th data which revealed an anticyclonic flow from at least 2007. However, our model does not reproduce the exact time when the circulation change. Therefore, combining the observations in the Barents Sea with the previous dense water analysis, I propose that, if the dense water recorded in 2002 entered the Arctic Ocean, it is possibly this source that triggered the anticyclonic flow in the Amerasian Basin.

Note that as release of the dense water plume requires multiple conditions, such as offshore (easterly) winds and large ice production events (Skogseth et al., 2005), the anticyclonic circulation pattern in the real Arctic should reverse, back to cyclonic, once the dense inflow decreases.

Also, because the dense water can be produced by ice formation and heat loss in the real world, this study suggests that whenever these (or similar) processes significantly increase the amount of dense water inflow, there is a potential to generate anticyclonic flow in the Amerasian Basin.

Finally, there is one question left to be answered: Exp. 2 corrected a precipitation error in the reference run. Why then is the circulation in Exp. 2 unable to reproduce the ^{230}Th observation?

As mentioned before, dense water on the shelf is mainly formed by the brine rejection during ice formation events, as in cold, polar regions, changes in salinity affect ocean density more than changes in temperature. I compared the amount of sea ice formation in both the observation and the simulation. The annual sea ice

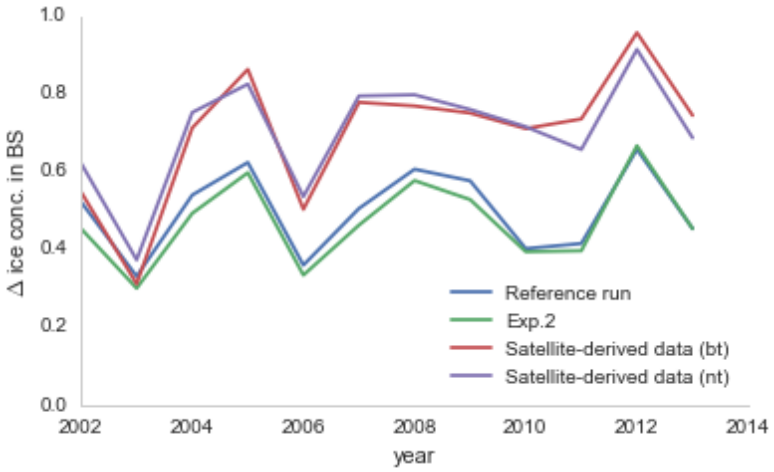

Figure 4.2: Sea ice formation events from observations and model in the period of 2002-2013. The red and purple lines show the change of sea ice concentration derived from satellite data using Bootstrap and NASA Team Algorithms respectively. The blue and green lines represents the increase in sea ice concentration from the reference run and the Exp. 2, respectively. Results indicate that, the ice formation predicted in the model is less than that from observations.

formation is approximated by subtracting the minimum sea ice condition (previous September) from maximum sea ice condition (March). Both sea ice concentrations from the Bootstrap (bt) and NASA team (nt) algorithms were used (Singarayer and Bamber, 2003). The sea ice formations computed from the nt and bt algorithms are similar and are much larger than those simulated by the model runs (Fig. 4.2). As such, we can conclude that there is less salt released in the modeled Barents Sea shelf region than in the real world.

For this reason, the amount of dense water in Exp. 2 is not sufficient to alter the shape of the Atlantic water isopycnals and thus is not able to alter the circulation. On the contrary, the lack of salt released from sea ice in the reference run is coincidently compensated by the effect of reduced precipitation.

It should be noted that we can not exclude the possibility that the drift of model salinity has an influence on the distribution of dense inflow, as the dense water inflow in the reference run is apparently too much. However, this possibility does not weaken our conclusion that an increase in dense water is the main reason for the circulation change.

4.3 Model limitations and perspectives

An unavoidable source of uncertainty is poor temporal and spatial coverage of Arctic observations. However, this factor is not within our control. During the construction of this model, several assumptions and extrapolations were made in order to use the limited data to establish an Arctic-wide model. This section will focus on discussing how those assumptions bring uncertainty into the simulated results.

The model uncertainty comes from the following steps:

- Biases related to circulation

Biases related to the physical field is the main reason why the model has a six-year delay in the increase of ^{230}Th concentration. Therefore, the biases related to the physical field can not be ignored. In order to predict a precise ^{230}Th map in the future, it will be essential to simulate an accurate flow field first. This could be achieved by improving the ice model as well as increasing the model resolution.

- Uncertainty in parameterizing scavenging coefficients

Uncertainty in parameterization is another source for the model uncertainty. There are three sources of uncertainty in parameterzing the scavenging coefficients.

First, the observation profiles under the high ice zone (over the Alpha Ridge and in the Makarov Basin) strongly deviate from linear. However, although I am aware that the non-linear shape of tracer profiles increases the uncertainty in the parameterization, limited data in the high ice region does not allow me to filter the unwanted stations.

Second, as lateral transport is ignored, the ^{230}Th based scavenging rates might be biased by assuming a one-dimensional model (Roy-Barman, 2009). For example, for a place that receives lateral transport from another place with higher ^{230}Th, the scavenging intensity would be underestimated; similarly, those affected by lower ^{230}Th water would be overestimated. Although the weak advection in Arctic justifies the method of using a one-dimensional model to estimate scavenging coefficients, this problem still generates potential uncertainty in this work. Also, we should note that in this one-dimensional model, we assume zero particulate concentration at the surface. Thus, this model does not take external sources (from sea ice or river or dust from atmosphere) into consideration. This has a larger influence on the particulate form than the dissolved form because the magnitude of a potential external source is small compared with the dissolved ^{230}Th concentrations.

Third, the uncertainty in the linear relationship between sea ice concentration and scavenging coefficients based on only two groups of observations can not be ignored. This uncertainty is probably the largest of the three. We can not exclude the possibility that the relationship between sea ice concentration and particle concentration might not always be linear. For example, it is very likely that the change in

scavenging coefficients might be flatter when the sea ice concentration is approaching 0 % and 100% and steeper in the middle (like an S-Curve). Also, there is only one particle type considered in the model. It is fair to believe that with more particle types included, approximations of the scavenging coefficients can be more accurate.

- Simplified in particle dynamics

The particle dynamics is another source of uncertainty. I did not consider aggregation/disaggregation/remineralization processes in the ice-particle model (2.11). The incomplete particle dynamics cycle leads to an inaccuracy in particle-related behavior and will be reflected in the tracer profile. This disadvantage will be exaggerated when it comes to the deeper ocean. For example, the break-down of biogenic particles in deep water, which may result in a noticeable decrease in the number of particles and thus a non-linear increase in the dissolved phase, will not be reproduced in the model. A more realistic particle dynamics in the ocean would be the largest area open for improvement in further modeling work.

Chapter 5

Summary

This work coupled a reversible scavenging model to an ocean flow field using NEMO v3.4 to model the water column distribution of dissolved and particulate ^{230}Th over the Arctic region. The three-dimensional ^{230}Th in Arctic is simulated for the first time. Due to the lack of particle fields in the model, I established an ice-particle model to approximate the particle distribution. The model is run from 2002-2020 with a 12-year spin-up period. Two sensitivity experiments were conducted to understand the simulated ^{230}Th behaviors, with one testing the impact from changes in circulation and the other testing the influence of changing particle fields caused by sea ice concentration variations.

The objective of this model work is to address the following research questions:

1. Can the model produce the observed change of ^{230}Th? What does the observed change imply about the Arctic circulation?

The model produced a reasonable spatial pattern that agrees with early measurements. During the run, this spatial pattern changed when the flow field in the reference run switched from cyclonic to anticyclonic in the intermediate layer of the Canada Basin. It resulted in a subsequent increase in simulated ^{230}Th concentration in the south Canada Basin. This change in simulated ^{230}Th concentration is consistent with the observed change. Thus it is fair to say that the model is successful in capturing the main feature of the ^{230}Th distribution.

Suggested by the tracer model, the observed change in ^{230}Th profile indicates the flow pattern in the Arctic Ocean has experienced a transition. Before 2007, intermediate circulation in the Canada Basin was cyclonic, which transported low ^{230}Th concentration towards the Alpha Ridge. In the late 2000s, the intermediate flow changed to an anticyclonic pattern. This change results in a reversal in ^{230}Th transport - high ^{230}Th concentrations from the Alpha Ridge was transported into the south Canada Basin. Consequently, measurements in 2009 documented an unusual, non-linear ^{230}Th profile.

The tracer model did not reproduce the exact year when the ^{230}Th increased and therefore it is difficult to derive conclusions on when the anticyclonic flow started. Judging by the ^{230}Th data only, the anticyclonic flow existed before 2007.

2. What's the reason for circulation changes in the Arctic?

There are two processes that contribute to circulation changes: local wind and

remote inflow.

The influence of wind occurs on a relatively short time scale (in less than a year) but the persistently decreasing topostrophy adjustment occurred over a much longer time scale. As such, the reversal of topostrophy sign is a result of an increase dense inflow from Fram Strait and, mainly, from the Barents Sea. The increase of dense water inflow alters the density distribution in the Arctic. A lift of isopycnals generates an internal Kelvin wave which carries an anticyclonic signal to the Amerasian Basin. The source of the dense water is located in the Barents Sea. The increase of dense water source is probably caused by enhanced ice formation over the Barents Sea.

There was a large ice formation event, together with the highest-ever recorded bottom salinity, observed in 2002 in the Barents Sea region (Skogseth et al., 2005). It is possible that the change in intermediate circulation was triggered by this event.

As this three-dimensional Arctic ^{230}Th model is established for the first time, this study also highlighted some limitations/difficulties in accurately simulating the tracer distribution. Future improvement can focus on two aspects: first, improving the scavenging model by finding a more realistic particle distribution through a more comprehensive relation between sea ice and biology productivity and by developing of a more complete particle cycle; second, improving the physical field by better parameterizing the ice model and increasing the model resolution. Regarding the shift in the intermediate circulation, this work was not able to resolve the sensitivity of the intermediate circulation to the increasing amount of dense water inflow. More simulation experiments that explore the relationship between the amount of dense water inflow and the dynamics of the intermediate layer are required to fully understand the response mechanism.

Since the intermediate layer is crucial to the overturning circulation and this thesis has proven that the flow pattern in this layer has significantly changed, one can speculate that the outflow from the Arctic Ocean would be saltier and stronger as a way to balance the intensified dense water inflow. If this is the case, the overturning circulation would be driven by a higher pole-to-tropics density contrast, with the condition that the density field in the tropical region experiences no significant change. Thus, instead of slowing down due to a decreasing contrast in the temperature field under a warming scenario, the future overturning circulation could possibly be strengthened as a result of the larger density contrast. Moreover, the shift in the overall circulation pattern of the intermediate layer is expected to produce changes in the heat distribution in the Arctic Ocean. Further exploration of the heat balance in the context of a new established intermediate circulation scheme would greatly contribute to the understanding of Arctic Ocean dynamics.

Bibliography

Aagaard, K. (1989). *A synthesis of the Arctic ocean circulation.* International Council for the Exploration of the Sea (ICES).

Bacon, M. P. and Anderson, R. F. (1982). Distribution of thorium isotopes between dissolved and particulate forms in the deep sea. *Journal of Geophysical Research: Oceans*, 87(C3):2045–2056.

Bacon, M. P., Huh, C.-A., and Moore, R. M. (1989). Vertical profiles of some natural radionuclides over the Alpha Ridge, Arctic Ocean. *Earth and Planetary Science Letters*, 95(1-2):15–22.

Blanke, B. and Raynaud, S. (1997). Kinematics of the Pacific equatorial undercurrent: An Eulerian and Lagrangian approach from GCM results. *Journal of Physical Oceanography*, 27(6):1038–1053.

Brown, Z. W. and Arrigo, K. R. (2012). Contrasting trends in sea ice and primary production in the Bering Sea and Arctic Ocean. *ICES Journal of Marine Science: Journal du Conseil*, 69(7):1180–1193.

Dai, A. and Trenberth, K. E. (2002). Estimates of freshwater discharge from continents: Latitudinal and seasonal variations. *Journal of hydrometeorology*, 3(6):660–687.

Delworth, T., Clark, P., Holland, M., Johns, T., Kuhlbrodt, T., Lynch-Stieglitz, C., Seager, R., Weaver, A., Zhang, R., et al. (2008). The potential for abrupt change in the Atlantic Meridional Overturning Circulation.

Döös, K. (1995). Interocean exchange of water masses. *Journal of Geophysical Research: Oceans*, 100(C7):13499–13514.

Dutay, J.-C., Lacan, F., Roy-Barman, M., and Bopp, L. (2009). Influence of particle size and type on ^{231}Pa and ^{230}Th simulation with a global coupled biogeochemical-ocean general circulation model: A first approach. *Geochemistry, Geophysics, Geosystems*, 10(1).

Edmonds, H. N., Moran, S. B., Hoff, J. A., Smith, J. N., and Edwards, R. L. (1998). Protactinium-231 and thorium-230 abundances and high scavenging rates in the western Arctic Ocean. *Science*, 280(5362):405–407.

Francois, R. and Soon, M. (2010). Dramatic changes in the dissolved ^{230}Th concentration of seawater in Canada Basin between 1995 and 2009: a transient Arctic circulation signal? In *EGU General Assembly Conference Abstracts*, volume 12, page 2989.

Henderson, G. and Wilkinson, J. (2012). Global database of literature and unpublished water column Pa and Th data. Retrieved from http://climotope.earth.ox.ac.uk/data_compilations/water-column_th_and_pa_dataset_notes_and_references.

Holdsworth, A. M. and Myers, P. G. (2015). The Influence of high-frequency atmospheric forcing on the circulation and deep convection of the Labrador Sea. *Journal of Climate*, 28(12):4980–4996.

Holloway, G., Dupont, F., Golubeva, E., Häkkinen, S., Hunke, E., Jin, M., Karcher, M., Kauker, F., Maltrud, M., Maqueda, M., et al. (2007). Water properties and circulation in Arctic Ocean models. *Journal of Geophysical Research: Oceans*, 112(C4).

Ivanov, V. and Watanabe, E. (2013). Does Arctic sea ice reduction foster shelfbasin exchange? *Ecological Applications*, 23(8):1765–1777.

Karcher, M., Kauker, F., Gerdes, R., Hunke, E., and Zhang, J. (2007). On the dynamics of Atlantic Water circulation in the Arctic Ocean. *Journal of Geophysical Research: Oceans*, 112(C4).

Karcher, M., Smith, J. N., Kauker, F., Gerdes, R., and Smethie, W. M. (2012). Recent changes in Arctic Ocean circulation revealed by iodine-129 observations and modeling. *Journal of Geophysical Research: Oceans*, 117(C8).

Kim, M., Hwang, J., Kim, H. J., Kim, D., Yang, E. J., Ducklow, H. W., La Hyoung, S., Lee, S. H., Park, J., and Lee, S. (2015). Sinking particle flux in the sea ice zone of the Amundsen shelf, Antarctica. *Deep Sea Research Part I: Oceanographic Research Papers*, 101:110–117.

Ku, H. (1966). Notes on the use of propagation of error formulas. *Journal of Research of the National Bureau of Standards*, 70(4).

Lerner, P., Marchal, O., Lam, P. J., Anderson, R. F., Buesseler, K., Charette, M. A., Edwards, R. L., Hayes, C. T., Huang, K.-F., Lu, Y., et al. (2016). Testing models of thorium and particle cycling in the ocean using data from station GT11-22 of the US GEOTRACES North Atlantic section. *Deep Sea Research Part I: Oceanographic Research Papers*, 113:57–79.

Lique, C., Johnson, H. L., and Davis, P. E. (2015). On the interplay between the circulation in the surface and the intermediate layers of the Arctic Ocean. *Journal of Physical Oceanography*, 45(5):1393–1409.

Lique, C., Treguier, A.-M., Blanke, B., and Grima, N. (2010). On the origins of water masses exported along both sides of Greenland: A Lagrangian model analysis. *Journal of Geophysical Research: Oceans*, 115(C5).

Luo, Y. and Lippold, J. (2015). Controls on ^{231}Pa and ^{230}Th in the Arctic Ocean. *Geophysical Research Letters*, 42(14):5942–5949.

Marchal, O., François, R., and Scholten, J. (2007). Contribution of ^{230}Th measurements to the estimation of the abyssal circulation. *Deep Sea Research Part I: Oceanographic Research Papers*, 54(4):557–585.

Marchal, O., François, R., Stocker, T. F., and Joos, F. (2000). Ocean thermohaline circulation and sedimentary 231Pa/230Th ratio. *Paleoceanography*, 15(6):625–641.

McLaughlin, F. A., Carmack, E. C., Williams, W. J., Zimmermann, S., Shimada, K., and Itoh, M. (2009). Joint effects of boundary currents and thermohaline intrusions on the warming of Atlantic water in the Canada Basin, 1993–2007. *Journal of Geophysical Research: Oceans*, 114(C1).

Meier, W., Fetterer, F., Savoie, M., Mallory, S., Duerr, R., and Stroeve, J. (2013). NOAA/NSIDC Climate Data Record of Passive Microwave Sea Ice Concentration, Version 2. *ID, Boulder, Colorado, USA*.

Oziel, L., Sirven, J., and Gascard, J.-C. (2016). The Barents Sea frontal zones and water masses variability (1980–2011). *Ocean Science*, 12(1):169–184.

Peng, G., Meier, W., Scott, D., and Savoie, M. (2013). A long-term and reproducible passive microwave sea ice concentration data record for climate studies and monitoring. *Earth System Science Data*, 5(2):311–318.

Pnyushkov, A. V., Polyakov, I. V., Ivanov, V. V., and Kikuchi, T. (2013). Structure of the Fram Strait branch of the boundary current in the Eurasian Basin of the Arctic Ocean. *Polar Science*, 7(2):53–71.

Roy-Barman, M. (2009). Modelling the effect of boundary scavenging on Thorium and Protactinium profiles in the ocean. *Biogeosciences*, 6(12):3091–3107.

Rudels, B. and Friedrich, H. J. (2000). The transformations of Atlantic water in the Arctic Ocean and their significance for the freshwater budget. In *The freshwater budget of the Arctic Ocean*, pages 503–532. Springer.

Rudels, B., Jones, E., Anderson, L., and Kattner, G. (1994). On the intermediate depth waters of the Arctic Ocean. *The polar oceans and their role in shaping the global environment*, pages 33–46.

Rudels, B., Schauer, U., Björk, G., Korhonen, M., Pisarev, S., Rabe, B., and Wisotzki, A. (2013). Observations of water masses and circulation in the Eurasian Basin of the Arctic Ocean from the 1990s to the late 2000s. *OS Special Issue: Ice-Atmosphere-Ocean interactions in the Arctic Ocean during IPY: the Damocles project*, 9(1):147–169.

Scholten, J., Van Der Loeff, M. R., and Michel, A. (1995). Distribution of 230Th and 231Pa in the water column in relation to the ventilation of the deep Arctic basins. *Deep Sea Research Part II: Topical Studies in Oceanography*, 42(6):1519–1531.

Singarayer, J. S. and Bamber, J. L. (2003). EOF analysis of three records of sea-ice concentration spanning the last 30 years. *Geophysical Research Letters*, 30(5).

Skogseth, R., Fer, I., and Haugan, P. M. (2005). Dense-water production and overflow from an Arctic coastal polynya in Storfjorden. *The Nordic Seas: An Integrated Perspective*, pages 73–88.

Smith, G. C., Roy, F., Mann, P., Dupont, F., Brasnett, B., Lemieux, J.-F., Laroche, S., and Bélair, S. (2014). A new atmospheric dataset for forcing ice–ocean models: Evaluation of reforecasts using the Canadian global deterministic prediction system. *Quarterly Journal of the Royal Meteorological Society*, 140(680):881–894.

Spall, M. A. (2013). On the circulation of Atlantic Water in the Arctic Ocean. *Journal of Physical Oceanography*, 43(11):2352–2371.

Støylen, E. and Fer, I. (2014). Tidally induced internal motion in an Arctic fjord. *Nonlinear Processes in Geophysics*, 21(1):87–100.

Trimble, S., Baskaran, M., and Porcelli, D. (2004). Scavenging of thorium isotopes in the Canada Basin of the Arctic Ocean. *Earth and Planetary Science Letters*, 222(3):915–932.

Tukey, J. W. (1977). *Exploratory data analysis*. First Edition, Reading, Mass: Addison-Wesley Publishing Co.

Venchiarutti, C., Jeandel, C., and Roy-Barman, M. (2008). Particle dynamics study in the wake of Kerguelen island using thorium isotopes. *Deep Sea Research Part I: Oceanographic Research Papers*, 55(10):1343–1363.

Yang, J. (2005). The Arctic and subarctic ocean flux of potential vorticity and the Arctic Ocean circulation. *Journal of Physical Oceanography*, 35(12):2387–2407.

Yu, E.-F., Francois, R., Bacon, M., and Fleer, A. (2001). Fluxes of 230Th and 231Pa to the deep sea: Implications for the interpretation of excess 230Th and 231Pa/230Th profiles in sediments. *Earth and Planetary Science Letters*, 191(3):219–230.

Zhang, J. and Steele, M. (2007). Effect of vertical mixing on the Atlantic Water layer circulation in the Arctic ocean. *Journal of Geophysical Research: Oceans*, 112(C4).

Appendix A

Choice of sea ice concentration

There are two options to embed sea ice concentration into the tracer model. The first choice is to directly apply simulated sea ice results from the existing physical runs (Table 2.1). The alternative one is to use satellite-derived sea ice data from NOAA/NSIDC Climate Data Record dataset (Meier et al., 2013; Peng et al., 2013).

Holdsworth and Myers (2015) suggests that the model generally does a good job of representing sea ice in the Labrador Sea. However, while the simulated sea ice is reasonable in the Labrador Sea, it is less than satisfactory in the Arctic region. A data-model comparison shows that while the observed data only has high sea ice concentrations on the CAA side of the Canada Basin, the model has high sea ice concentration in the entire Canada Basin (Fig. A.1). Also, while the observed sea ice is thin in the shelf region, the model displays thick sea ice there. This result indicates that the spatial variation of the modeled sea ice deviates from the observations.

In this study, the variation of sea ice concentration is crucial in setting the scavenging intensity in the Arctic region, therefore, I chose observed sea ice data as model inputs.

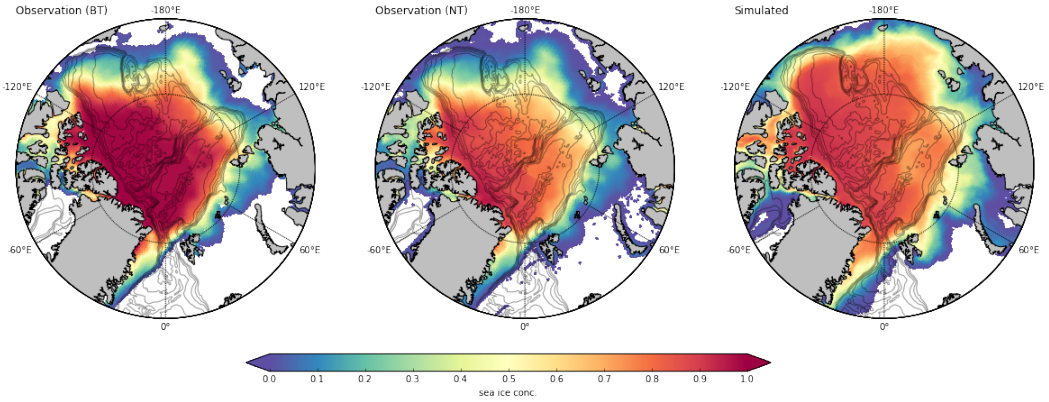

Figure A.1: Data-model comparison on average sea ice pattern from 2002-2014. From left to right: observations from (a) the NASA Team (NT), (b) Bootstrap (BT) algorithm and (c) the reference run. Result shows that the sea ice spatial pattern from the model deviates from the observations.

However, the observed sea ice dataset contains ice concentration products from

two well established algorithms: the NASA Team (NT) algorithm and the Bootstrap (BT) algorithm. Given that there are considerable differences in total ice covered area between these two products due to the difference in processing passive microwave radiation data, the following paragraphs discuss the choice between these products.

Previous work analyzes the ice products from these two algorithms using Empirical Orthogonal Function (EOF). Result indicates that, in general, the NASA team data produce lower ice concentrations than the Bootstrap. However, the major modes of variability derived from the EOF analysis from both products were essentially the same (Singarayer and Bamber, 2003).

To model the tracer distribution, variability in sea ice concentration is more important than absolute magnitude. As such, the high similarity of the most significant modes of variability makes the choice of dataset less critical. Considering that large areas of artificial-saturation observed in the BT records, I selected products from NT as sea ice inputs in this study.

Note that not all satellites pass close enough to the North Pole for their sensors to collect data there. This missing data around the North Pole is filled in by nearest-neighbor interpolation using Scipy.interpolate Python package.

Appendix B

Preliminary model

B.1 1D Model

The preliminary 1D model solves a system of coupled, linear equations. It is set up on a 1D domain with a zero background velocity field imposed. Steady state numerical solutions are compared with analytical solutions for consistency.

Initialized with zero concentration

With a hypothetical state of no advection, there is no lateral transport of ^{230}Th concentration. As such, for the steady state, the numerical solutions for ^{230}Th (in both forms) linearly increase in magnitude with depth (Fig. B.1: left and mid panels). The time required for tracers to reach steady state increases from surface to seafloor. The magnitudes of the numerical solutions are consistent with the analytical results.

Initialized with zero concentrations, the time for ^{230}Th at 1000 m depth to achieve steady state is approximately 18 years under the ice-free and and approximately 125 years under the permanent ice area. Both forms of tracer increase fast in concentrations for the first few years and their values slowly converge to the steady states (Fig. B.1: right panels).

Initialized with steady state ^{230}Th concentrations from low ice region

An interesting question to ask will be: if the ^{230}Th profiles were initialized with a steady state low ^{230}Th concentration from a low ice region, instead of zero concentration, how long it takes to build up high ^{230}Th values.

In this part, the initial ^{230}Th concentrations are generated from a ice-free, steady state ^{230}Th profile. Result shows that ^{230}Th at 1000 m depth spends approximately 125 years to reach a new steady state (Fig. B.2). This length of time is, surprisingly, not significantly shorter than that initialized with zero concentration (125$\sim$130 years). This quick experiment supports that the significant increase in observed ^{230}Th in such a short time scale (in less than 5 years) is not caused by a change in scavenging intensities.

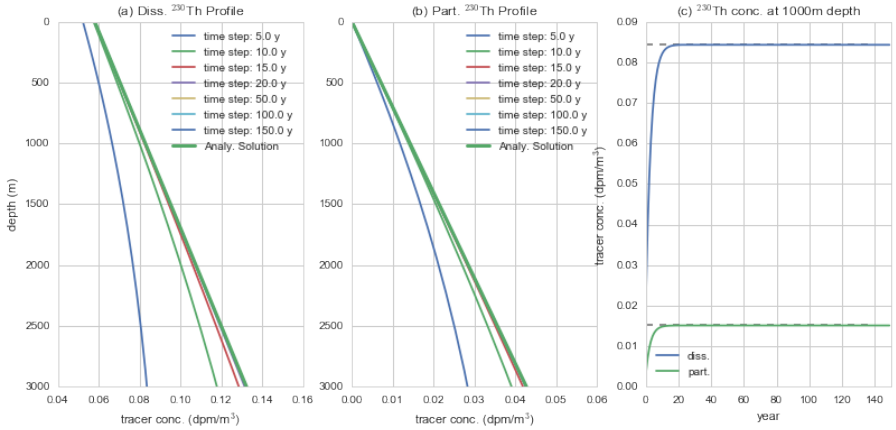

(a) under low ice condition

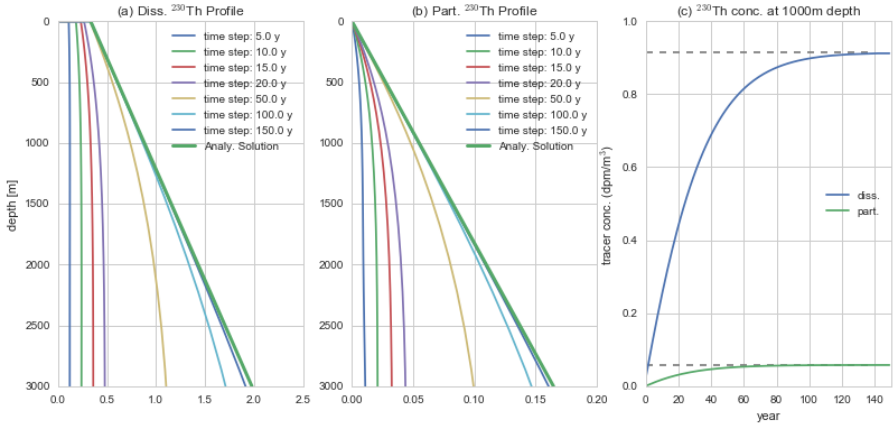

(b) under high ice condition

Figure B.1: Numerical solutions of one-dimensional ^{230}Th model without background velocity. The left and middle panels in (a) and (b) show the evolutions of ^{230}Th vertical profiles (dissolved and particulate, respectively) under different sea ice conditions. The right panels focus specifically on the evolutions at 1000 m depth, with gray lines indicating the steady state values. Results show that the steady state solutions in both phases propagate from surface to seafloor and that the time to reach steady state would be longer for profiles under a high ice condition.

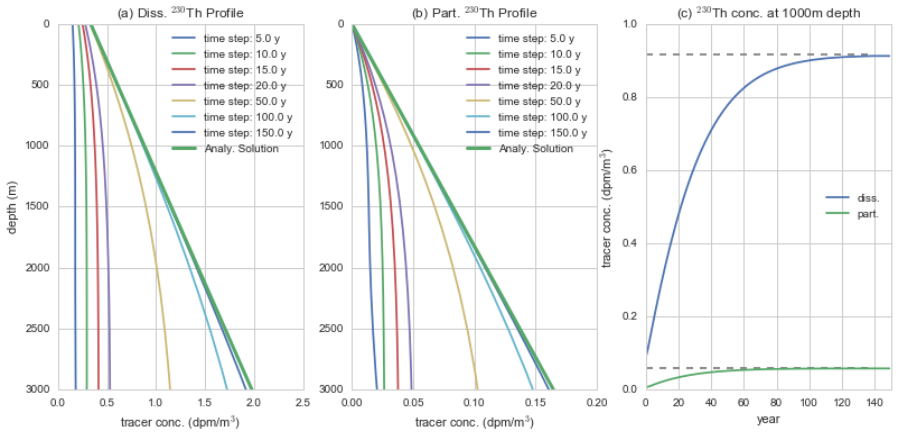

Figure B.2: Numerical solutions of one-dimensional ^{230}Th model without background velocity and with a steady state ^{230}Th concentration from low ice region. Panels structure is the same as Fig. B.1. The amount of time to reach steady state is found to be just slightly shorter than that initialized with zero concentration (<5 years).

B.2 2D Model

The 2D model not only adds an extra dimension to the 1D model, but also includes an addition process: the advection process. In this test, the model is forced by an idealized eastward constant flow. The model domain is 5000 m by 1000 km, with a 20 km horizontal resolution and a 100 m vertical resolution. The model is separated into two regions with different characteristics: the first 400 km in x direction is assumed to be covered by permanent ice; the rest (400 - 1000 km in x direction), however, is ice-free. Their scavenging rates are estimated with 100% and 0% ice concentration, respectively. This model is established to examine how the tracer distribution evolves with the advection process imposed.

With advection, tracer concentrations from the high ice region was advected to the low ice covered zone. With a constant 100 km y^{-1} velocity, the front of the high ^{230}Th concentration water mass (originally at x = 400 km) reached the right edge of the model boundary (at x = 1000 km) during the sixth year. The flow pathway is reflected by the movement of the high ^{230}Th.

Note that the high dissolved ^{230}Th concentration dissipated after it was transported to the ice free zone which has higher scavenging intensities. On the contrary, the particulate ^{230}Th gained large amounts of concentration from the huge drop in dissolved ^{230}Th concentration. In order to balance the decrease in dissolved ^{230}Th, the maximum particulate ^{230}Th concentration even exceeded that originally developed under the high ice region.

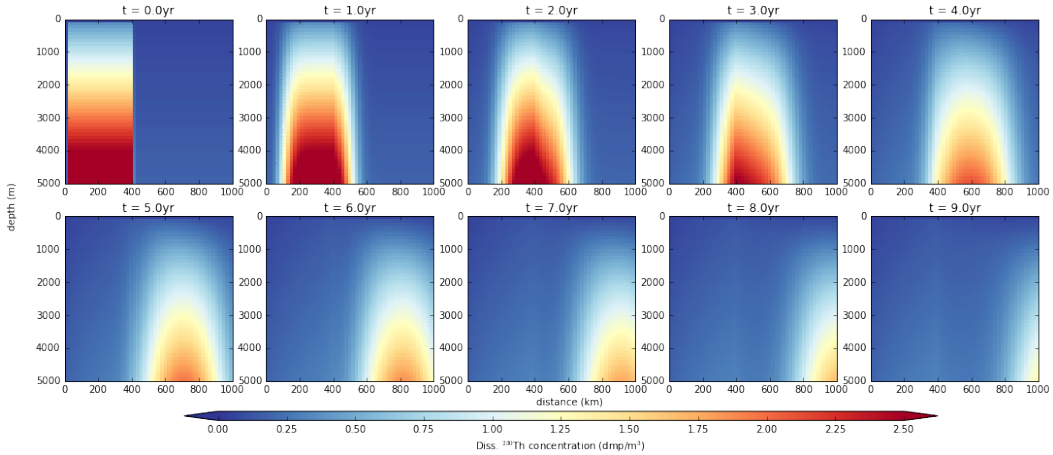

(a) dissolved ^{230}Th

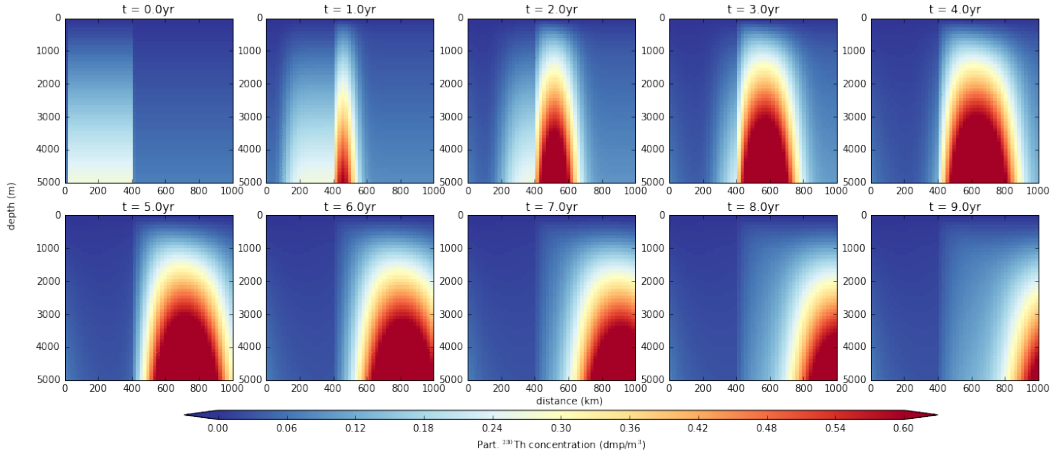

(b) particulate ^{230}Th

Figure B.3: Numerical solutions of two-dimensional ^{230}Th model, with a constant eastward background velocity imposed for ten model years. Consistent with modeled velocity speed (100 km y^{-1}), the front of the high ^{230}Th concentration water mass (originally at x = 400 km) reached the right edge of the model boundary (at x = 1000 km) during the sixth year. However, all panels similarly display significant increases in particulate ^{230}Th concentrations while the high ^{230}Th water masses are transported eastward.

Back to the high ice region, the scavenging rates are low enough to build up high ^{230}Th (in both phases). However, with continuous transport of low ^{230}Th water mass into the high ice zone (0-400 km in x direction), the high ^{230}Th concentration was not able to re-establish.

Appendix C

Physical model evaluation

This section conducted a quick evaluation on the performances of the physical model's salinity and temperature fields. The observed data used in the comparison is from the World Ocean Database (WOD). The evaluation focused on six Arctic sub-regions: the boundary of the Canada and Makarov basins, the internal Canada Basin, the interior of the central Arctic, the Kara sea opening and the Barents Sea opening (Fig. C.1). This comparison focuses on the intermediate layer: the data from 1000 ± 50 m were chosen; model results all from the 1000 m depth.

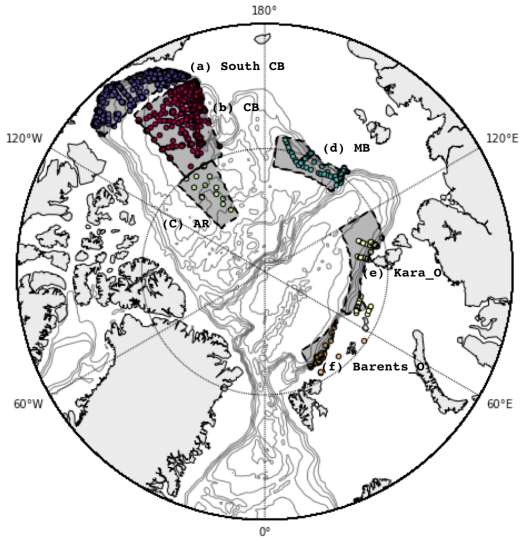

Figure C.1: Locations of the data-model comparison: the boundary of the Canada and Makarov basins, the internal Canada Basin, the internal of central Arctic, the Kara sea opening and the Barents Sea opening. Points indicate the sample locations.

The magnitude of simulated salinity compares very well with the observed salinity fields in both EXH001 and EXH005 (used in the reference run and Exp. 2, respectively). Observations suggest that there are large variations in the Makarov Basin and the Kara Sea opening. This feature is captured in the model. For the rest of the sub-domains, the modeled salinity also compares favorably to the observed salinity, which is in the range of 34.88-34.94.

For the temperature field, the largest variations are also seen in the Makarov

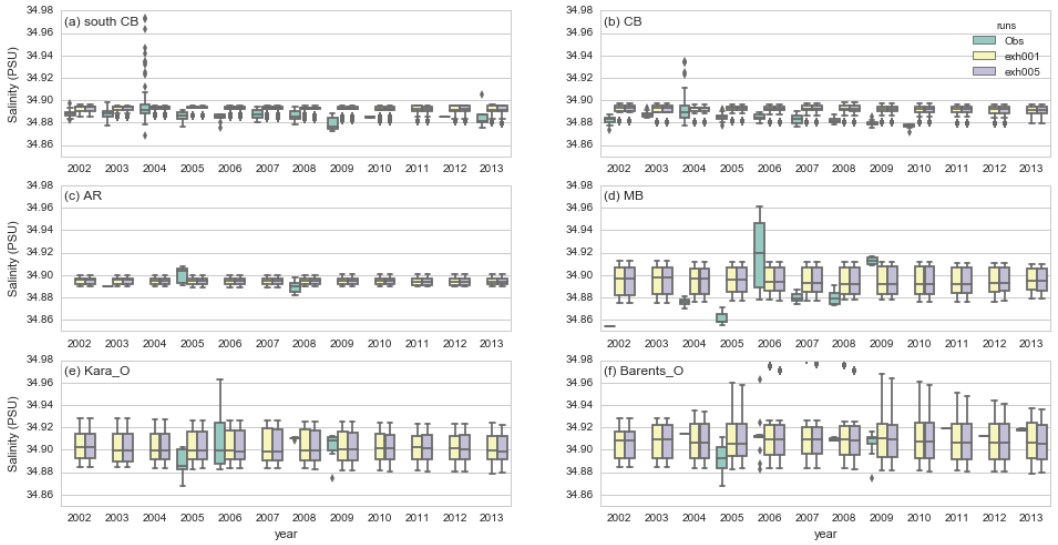

(I) salinity

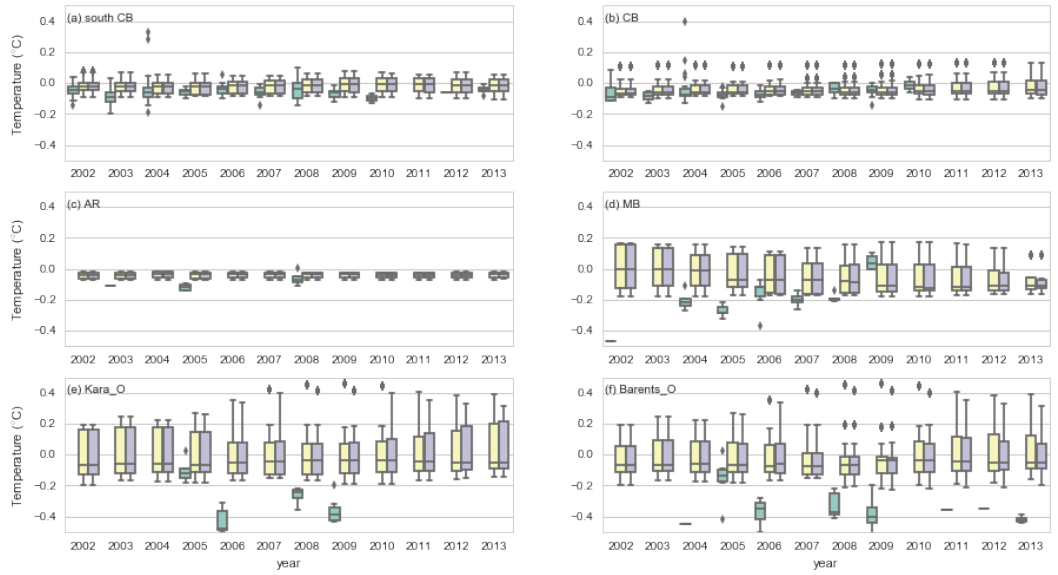

(II) temperature

Figure C.2: Physical model evaluations with respect to the observations from the World Ocean Database (WOD). The model simulations of the intermediate depth in six sub-domains are generally in line with observations.

Basin and in front of the Kara Sea and the Barents Sea openings. The results show that the magnitude of simulated temperature in both runs generally corresponds well to the observations with exceptions in the Kara Sea and the Barents Sea opening area. In this region, the simulated temperature is approximately 0.2-0.3 °C higher than that from observations. However, as the density/stratification in the Arctic, which includes the Kara Sea opening, is salinity-dominant, the influence caused by temperature deviations from the observations are limited. As such, it is fair to assume that the overall Arctic dynamics is not strongly affected.

There is a hardly noticeable feature revealed by this evaluation: the modeled salinity field in EXH001 is found to have higher values than that in EXH005. This difference mainly occurred in the Barents Sea and the Kara Sea openings. From the limited observations in the Barents Sea opening, slightly higher values of salinity field are found compared to those from the model. This result supports the previous argument that insufficient salt is released in the modeled Barents Sea region in EXH005.

Summarizing, the model simulations of the intermediate depth in six sub-domains are in line with observations and the model is fit for the purpose of the study.

Appendix D

^{231}Pa and ^{230}Pa/^{230}Th in the intermediate layer

In order to maintain consistency with the earlier ^{230}Th analysis (Chapter 3), the ^{231}Pa and ^{230}Pa/^{230}Th concentrations are shown in year 2007, 2009, 2015, 2020 at 1000 m depth for the reference run.

D.1 Dissolved ^{231}Pa

The model behavior of dissolved ^{231}Pa is almost the same as dissolved ^{230}Th during the model period (Fig. D.1). Due to this similarity, the ^{231}Pa results are put in this appendix for compactness and clarity of the thesis.

In phase I (2007), the highest concentration of dissolved ^{231}Pa was located in the Alpha Ridge area, with some low ^{231}Pa water masses from the Canada Basin extending cyclonicly along the basin boundary. In phase II (2009), the spatial pattern did not change significantly. A slight difference to 2007 is that the low ^{231}Pa water mass retreated back to the Canada Basin, rather than extending to the Alpha Ridge.

In phase III (2009) and IV (2015), it is clear that the high dissolved ^{231}Pa water masses moved from the Alpha Ridge, via the south Canada Basin, toward the Chukchi Plateau and the low ^{231}Pa concentration water moved toward the Makarov Basin and the central Arctic.

The high similarity between the ^{231}Pa and ^{230}Th evolution suggests that both of the tracers are similarly affected by lateral transports and scavenging.

The change in the highest ^{231}Pa location, as well as the change in the low ^{231}Pa water propagation direction, suggests the flow pattern reversed from cyclonic to anticyclonic during the model period. This result is consistent with that revealed by the ^{230}Th simulation.

Unfortunately, ^{231}Pa observations in the Canada Basin are only available in 2007 and 2015, but not in 2009 when the high ^{230}Th concentrations were detected. However, given the similarity in the ^{230}Th and ^{231}Pa cycles, one can expect that the increase in ^{231}Pa concentration found in phase III and IV is a real feature.

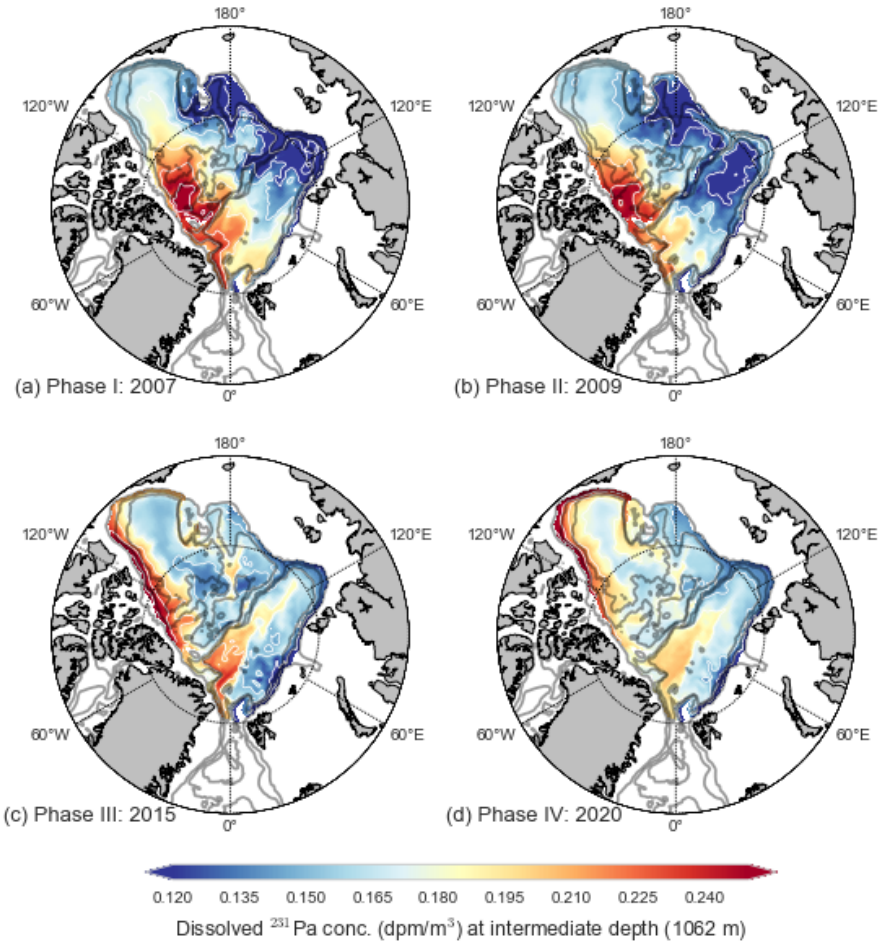

Figure D.1: Horizontal distribution of simulated dissolved ^{231}Pa concentration in the intermediate layer. Results are displayed in phase (a) I (2007), (b) II (2009), (c) III (2015) and (d) IV (2020). Tracer concentrations shown here are annually averaged model results. High concentrations seen in phase I (2007) and phase II (2009) moved southward along the CAA in phase III (2015) and dissipated in phase IV (2020).

D.2 Particulate ^{231}Pa

The evolution of particulate ^{231}Pa exhibited a similar pattern to that of particulate ^{230}Th. In phase I (2007) and II (2009), the highest particulate ^{231}Pa was found under the seasonally ice-free area in the Canada Basin. Intermediate particulate ^{231}Pa concentration water was located over the Alpha Ridge. The Eurasian Basin and the south Makarov Basin had low particulate ^{231}Pa water masses.

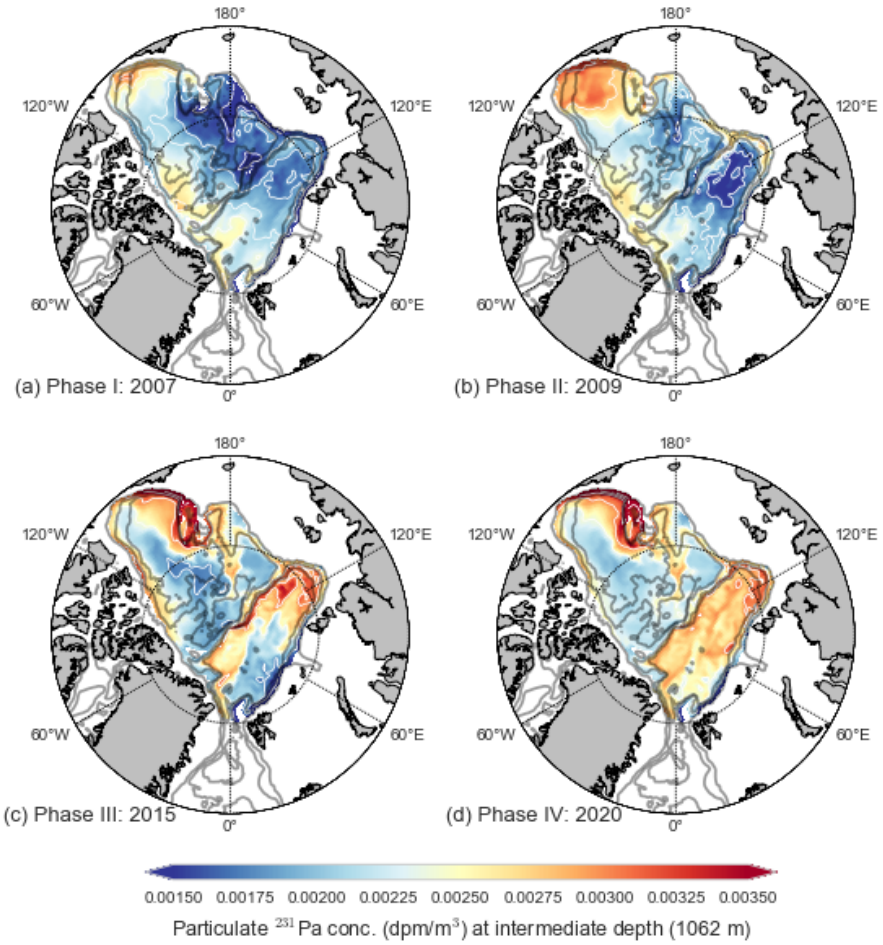

Figure D.2: Horizontal distribution of simulated particulate ^{231}Pa concentration in the intermediate layer. Results are displayed in phase (a) I (2007), (b) II (2009), (c) III (2015) and (d) IV (2020). There was an domain-wide increase in the particulate ^{231}Pa concentration, with the high particulate ^{231}Pa constrained to the Chukchi Plateau side of the Canada Basin in phase III and IV.

In phase III (2015) and IV (2020), the particulate ^{231}Pa experienced an Arctic-wide increase. The previous low ^{231}Pa in the Eurasian Basin and the south Makarov Basin increased to an intermediate level. Meanwhile, high particulate ^{231}Pa concentrations were more constrained to the Chukchi Plateau side of the Canada Basin. This spatial pattern is different from the ice-type particle field, which suggests an advection signal. Unfortunately, I do not have particulate ^{231}Pa data to evaluate this change at this stage.

D.3 Dissolved ^{231}Pa/^{230}Th

The distribution of dissolved ^{231}Pa/^{230}Th is, again, similar to the spatial pattern in dissolved ^{230}Th, but reversed. Where the ^{230}Th concentration is high, the ^{231}Pa/^{230}Th ratio turns out to be low (as ^{230}Th is the denominator). In phase I, a high ^{231}Pa/^{230}Th pool occurred in the Canada Basin, with a noticable north-west trend towards the Alpha Ridge. The rest of the Arctic mainly consisted of low ^{231}Pa/^{230}Th water because of the relatively low scavenging intensities which were caused by high sea ice condition.

The spatial pattern in phase II did not change significantly as compared to phase I. However, the north-west spread of the high ^{231}Pa/^{230}Th terminated. The high ^{231}Pa/^{230}Th poll retreated back to the south Canada Basin. Meanwhile, due to a sharp decrease in sea ice concentration at the east Arctic Ocean, the ^{231}Pa/^{230}Th in the south Makarov Basin and the Russia side of the Eurasian Basin increased.

Phase III depicts a significant change in the ^{231}Pa/^{230}Th field. The high ^{231}Pa/^{230}Th water now moved east from the south Canada Basin, through the Chukchi Plateau , to the Makarov Basin. The low ^{231}Pa/^{230}Th water over the Alpha Ridge was moved southward to fill the south Canada Basin. Meanwhile, an intermediate ^{231}Pa/^{230}Th water developed in the Eurasian Basin.

The spatial pattern in phase IV further evolved and became less similar to that in dissolved ^{230}Th. In this phase, low ^{231}Pa/^{230}Th occurred in the Canada Basin and over the Alpha Ridge, while high ^{231}Pa/^{230}Th occupied the Makarov Basin and medium ^{231}Pa/^{230}Th dominated the Eurasian Basin. This pattern reflected three main gyres in the intermediate circulation.

The difference in spatial pattern between dissolved ^{230}Th and ^{231}Pa/^{230}Th supports the idea that ^{231}Pa/^{230}Th is a useful tool for larger scale circulation. However, because the residence time of the Arctic Ocean intermediate water is relatively short as compared to the tracers', the usefulness of ^{231}Pa/^{230}Th is limited as its spatial variation can be very quickly homogenized (eg. Fig. D.3).

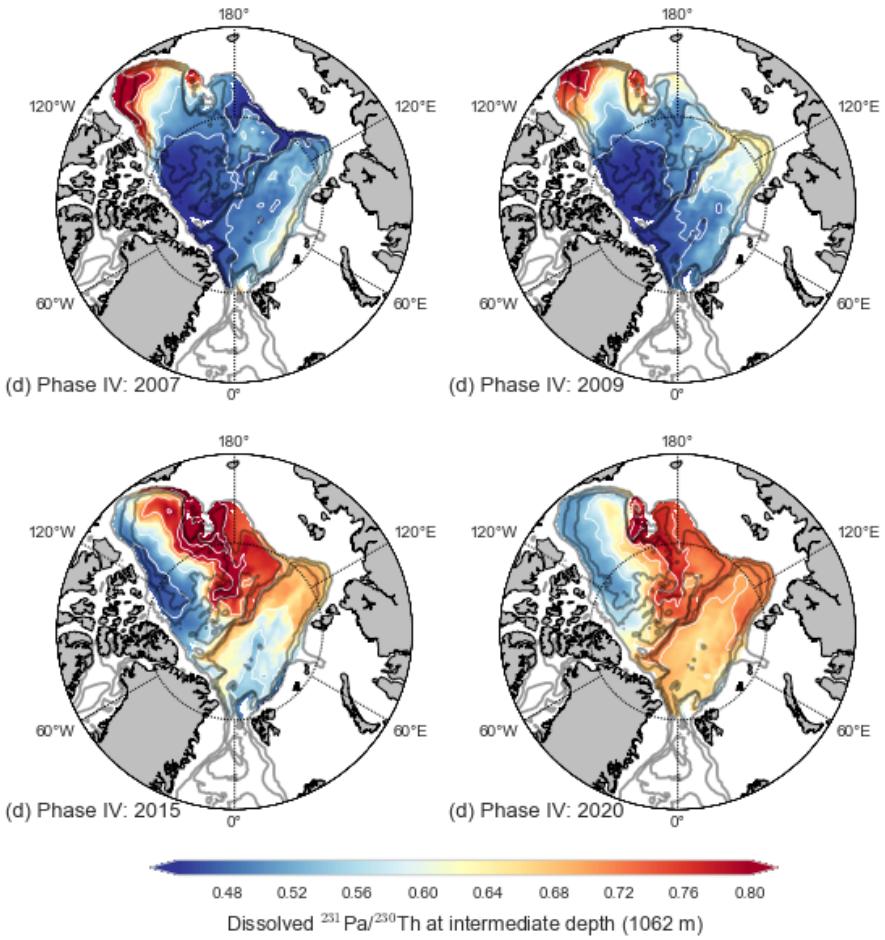

Figure D.3: Horizontal distribution of simulated particulate $^{231}Pa/^{230}Th$ concentration in the intermediate layer. Results are displayed in phase (a) I (2007), (b) II (2009), (c) III (2015) and (d) IV (2020). Tracer concentrations shown here are annually averaged model results. High concentrations seen in phase I (2007) and phase II (2009) moved anticyclonic to the Chukchi Plateau side of the Canada Basin in phase III (2015) and dissipated in Phase IV (2020).

D.4 Particulate $^{231}Pa/^{230}Th$

Evolution of the particulate $^{231}Pa/^{230}Th$ is consistent with that seen in the dissolved $^{231}Pa/^{230}Th$ (Fig. D.4). Similar to dissolved $^{231}Pa/^{230}Th$, a spread of high $^{231}Pa/^{230}Th$ was seen in the Canada Basin in phase I (2007). It extended north-west into the Alpha Ridge region. Meanwhile, a transport of low $^{231}Pa/^{230}Th$ water from the Eurasian Basin to the Amerasian Basin was observed in the simulation.

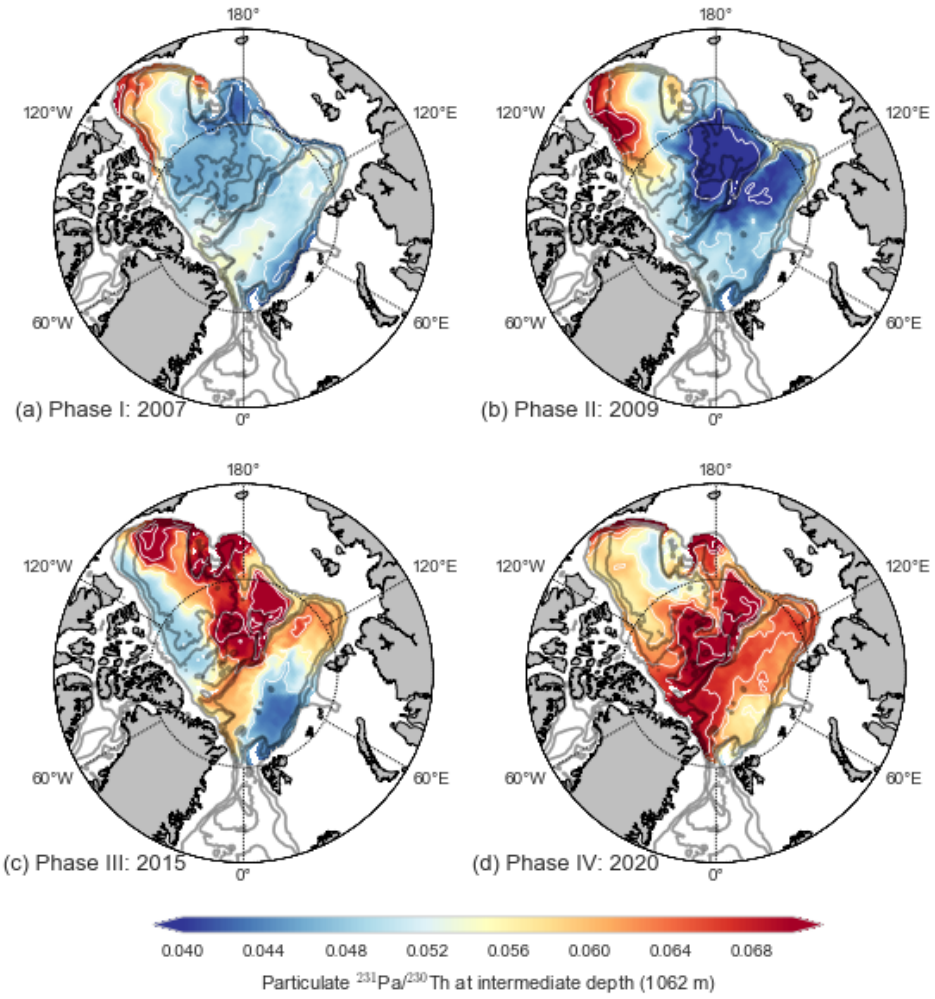

Figure D.4: Simulated particulate $^{231}Pa/^{230}Th$ concentration in phase (a) I (2007), (b) II (2009), (c) III (2015) and (d) IV (2020). The high particulate $^{231}Pa/^{230}Th$ water originally propagated northward toward the Alpha Ridge but finally accumulated in the Makarov Basin.

In phase II (2009), the north-west spread of high $^{231}Pa/^{230}Th$ water in the Canada Basin discontinued. A significant amount of low $^{231}Pa/^{230}Th$ water from the Eurasian Basin was transported further into the central Arctic.

Phase III (2015) shows that the low $^{231}Pa/^{230}Th$ concentration pool traveled along the Canada side of the Alpha Ridge and arrived in the south Canada Basin. The change in spatial pattern was also witnessed by the shift in the high $^{231}Pa/^{230}Th$ pool location, which was seen in both the south Canada Basin and in the Makarov Basin.

Phase IV (2020) indicates an increase in overall $^{231}Pa/^{230}Th$ values due to thin-

ner sea ice condition. However, if we focus on the spatial pattern instead of the absolute value, the reader can find that the particulate ^{231}Pa/^{230}Th was relatively low in the Canada Basin; very high in the Makarov Basin and intermediate in the Eurasian Basin. These three different particulate ^{231}Pa/^{230}Th water masses coincided with three intermediate depth circulation loops. This result is similar with that inferred from the dissolved ^{231}Pa/^{230}Th.

Appendix E

Tracer distribution in deep layer

E.1 Dissolved ^{231}Pa and ^{230}Th

Water beneath the intermediate layer is considered as the deep layer. Tracer concentrations from a depth of 3000 m are chosen to present model results for this layer.

Among the limited observations in deep water, there is no significant changes observed (Fig. 3.5). Here, the year 2002, 2007 and 2015 are chosen to represent the tracer pattern before, during and after the intermediate flow pattern changes.

The dissolved ^{231}Pa and ^{230}Th distributions in 2002 (before the shift in the intermediate layer occurred) showed the Canada Basin, the Makarov Basin and the Eurasian Basin contained the lowest, the highest and intermediate values in both ^{230}Th and ^{231}Pa concentrations, respectively (Fig. E.1).

The spatial pattern in 2007, when the shift in the intermediate circulation occurred, did not significantly change as compared to 2002. The main differences were seen in the low ^{230}Th and ^{231}Pa concentration tongues, which extended further north toward the Alpha Ridge.

In 2015 after the intermediate change happened, the low concentration tongue still existed along the boundary of the Canada Basin; however, instead of moving north-west toward the Alpha Ridge side, it extended all the way to the Chukchi Plateau. Meanwhile, the high ^{230}Th and ^{231}Pa at this layer decreased dramatically in the Makarov and Eurasian basins. However, unlike tracers in the intermediate layer, there were not high tracer concentration tongues developed at this depth.

Since the velocity is slow (approximately 0.002m s^{-1}) in the deep layer, the advection effect is small as compared to the upper ocean. It is likely that the 2015 pattern is caused by the sinking from the intermediate layer. The scavenging process dominates the deep ocean tracer distribution.

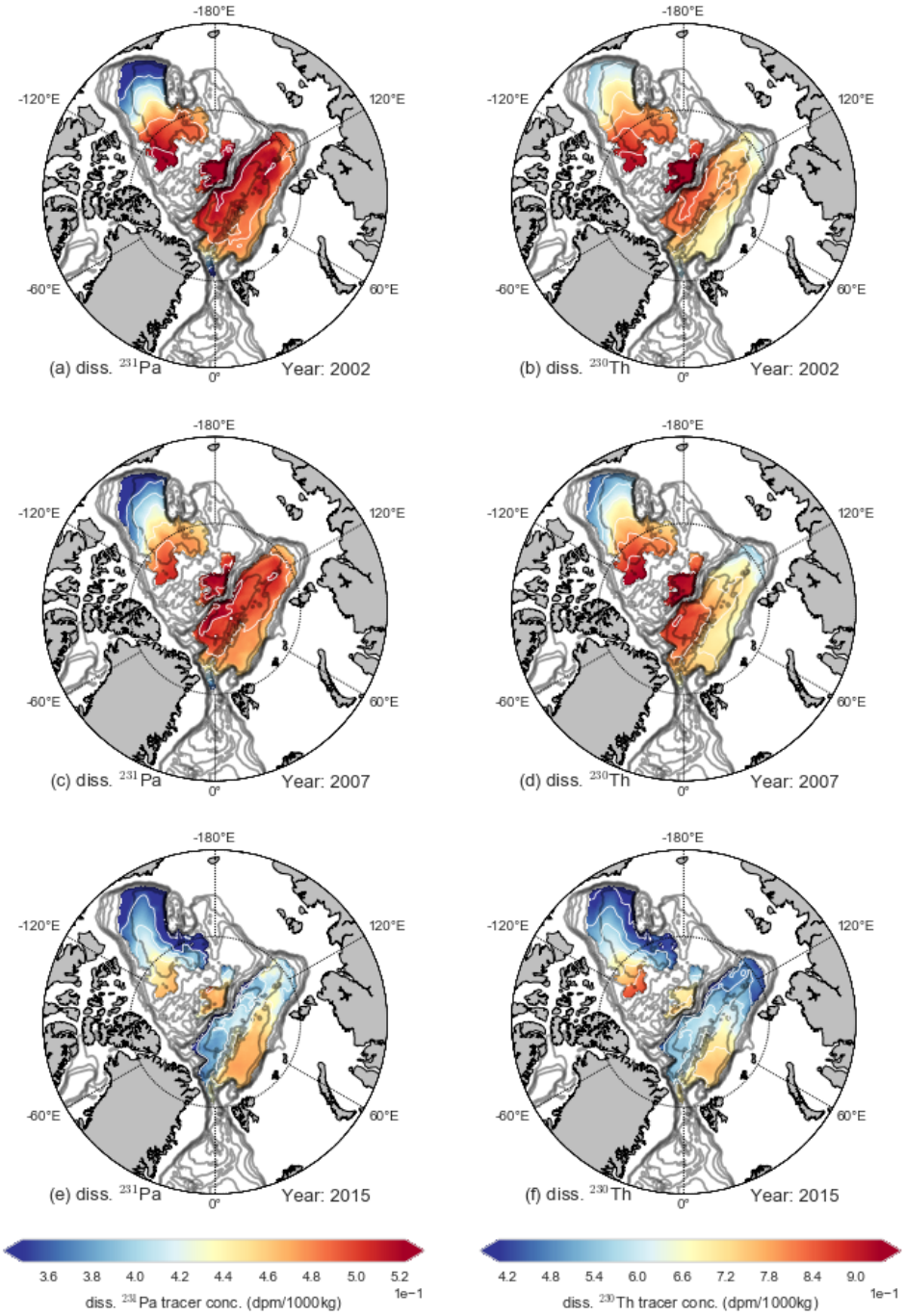

Figure E.1: Simulated dissolve ^{231}Pa and ^{230}Th concentration in year (a,b) 2002, (c,d) 2007 and (e,f) 2015. The low tracer concentrations in the south Canada Basin found in 2002 and 2007 extended to the Chukchi Plateau side of the Canada Basin in 2015.

E.2 Particulate ^{231}Pa and ^{230}Th

Result shows that, in 2002, the high concentrations of both particulate ^{230}Th and ^{231}Pa were constrained to the Chukchi Plateau side of the seasonally ice-free Canada Basin (Fig. E.2). In 2007 and 2015, these zones dissipated but relatively high ^{230}Th and ^{231}Pa concentration could still be seen on the Chukchi Sea side of the Canada Basin. Again, there were no high particulate tracer tongues seen at this depth.

E.3 Ratio of ^{231}Pa/^{230}Th

Surprisingly, while the dissolved and particulate ^{231}Pa and ^{230}Th distributions only provide obscure circulation patterns, their ratios indicated a clear cyclonic movement of the ^{231}Pa/^{230}Th ratio in the Canada Basin in 2007, from the south Canada Basin to the west basin along the boundary of the CAA; and an anticyclonic movement in 2015, revealed by the east-moving high ^{231}Pa/^{230}Th tongues from the south Canada Basin to the Chukchi Plateau side of the Canada Basin. Such change suggests that the Arctic, to be specific, the Canada Basin, experienced a significant change in circulation pattern.

However, as the deep layer receives plenty of sinking particles from the upper ocean, it is hard to quantify how much of the change in tracer concentration was caused by the intermediate layer. It therefore appears difficult to derive some definitive conclusions upon the behavior of the trace elements from these results.

As for the Eurasian Basin, the high ^{231}Pa/^{230}Th moved in a cyclonic pattern over the model period. As a result, one can expect there is no significant change in flow field in this (and the intermediate) layer.

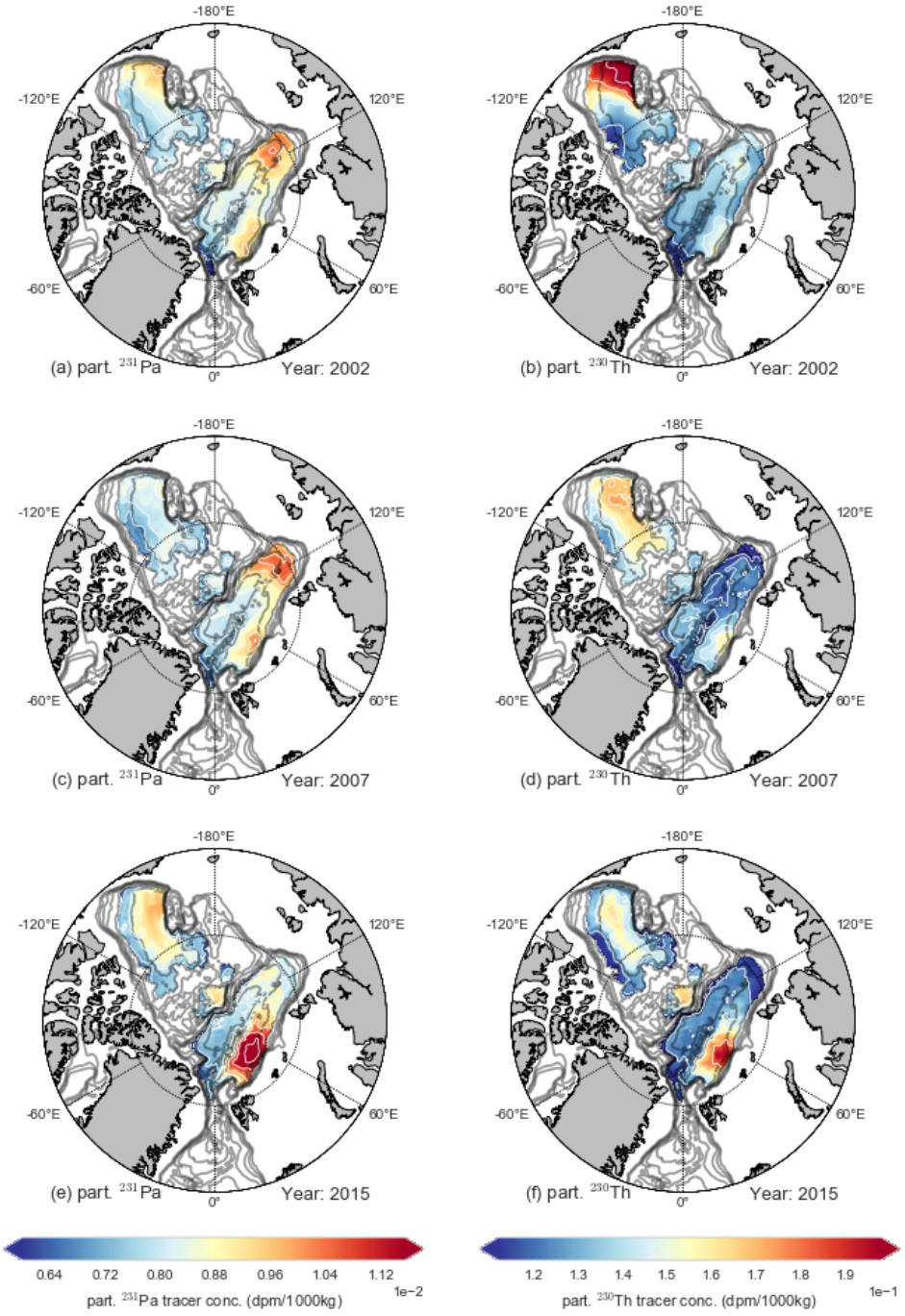

Figure E.2: Simulated particulate ^{231}Pa and ^{230}Th concentration in year 2002 (a)(b), 2007 (c)(d) and 2015 (e)(f). High tracer concentrations zones over the south edge of the Canada Basin found in 2002 spread into the central Canada Basin in the 2007 and 2015.

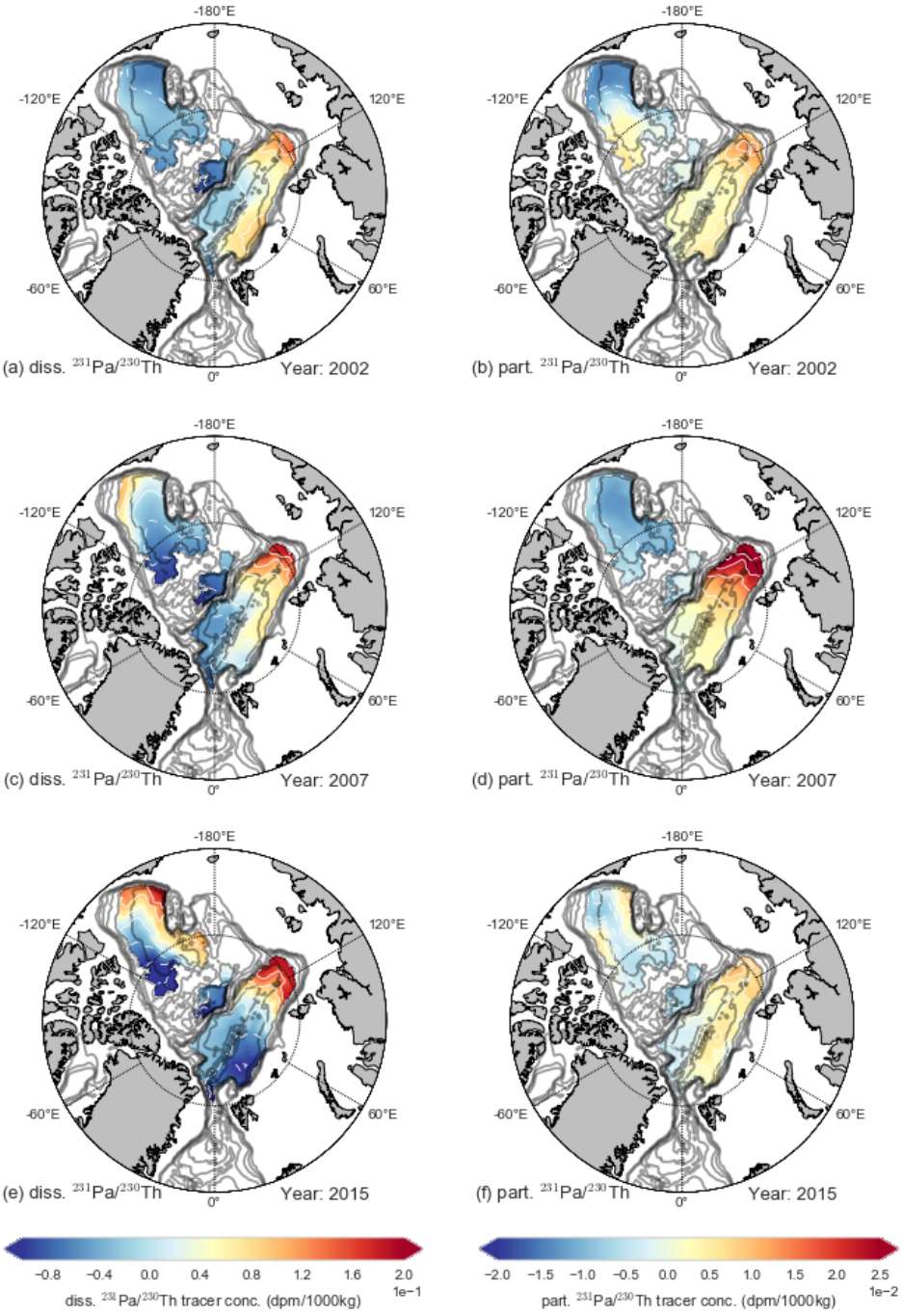

Figure E.3: Simulated dissolve and particulate $^{231}Pa/^{230}Th$ concentration in year 2002 (a)(b), 2007 (c)(d) and 2015 (e)(f). In the Canada Basin, a high ratio zone developed along the CAA side in 2007 then it flowed along the south edge of the Canada Basin to the Chukchi Plateau side in 2015.